PREDICTION AND EXPERIMENTAL EVALUATION OF PLANAR WING SPANLOADS FOR MINIMUM DRAG

BY

GABRIELLE WROBLEWSKI

THESIS

Submitted in partial fulfillment of the requirements
for the degree of Master of Science in Aerospace Engineering
in the Graduate College of the
University of Illinois at Urbana-Champaign, 2016

Urbana, Illinois

Adviser:

Assistant Professor Phillip Ansell

Abstract

Optimum wing spanloads were evaluated by comparing wing performance values from theoretical predictions and experimental wind-tunnel measurements. The optimum spanloads were found using a Lagrange multiplier optimization method. They were designed with a prescribed wing-root bending moment constraint with and without incorporating viscous representation. Wind-tunnel models were created based on the optimum spanloads and the experiments were conducted to evaluate the changes in drag as the design constraints differed. The results indicate that an optimized spanload having equal lift and wing-root bending moment to that of an elliptically-loaded wing can experience significant decreases in drag. Comparisons between the theoretical predictions and the wind-tunnel models were made using experimental 5-hole probe wake-survey measurements, which were reduced into total lift and drag, as well as spanwise lift distributions.

Thanks to my parents for all their love and hard work getting me here,

To Mike for believing in me, always. Love yah, bug.

And to Bub and Cooper for being the best friends a gal could ever ask for.

Acknowledgements

Many thanks to Professor Phillip Ansell for guidance and support, and for the opportunity to work on this rad project. Support for this work was provided through the Department of Aerospace Engineering at Illinois, as well as NASA STTR Contract No. NNX14CD17C. Thanks to Mike Kerho, Kurt Kloesel, Hyun Dae Kim, Albion Bowers, and the staff of NASA Armstrong Flight Research Center for their contributions to this work.

Additional thanks to Phil Ansell, as well as Jeff Diebold and Brent Pomeroy for teaching me how to carry out wind tunnel experiments.

Table of Contents

List of Figures

List of Tables

Nomenclature

A_{ij}	=	aerodynamic influence coefficient matrix
AR	=	aspect ratio
b	=	span
c	=	local wing chord
c_{avg}	=	mean geometric chord
$\bar{c}$	=	mean aerodynamic chord
C_d	=	sectional drag coefficient
C_D	=	wing drag coefficient
C_l	=	sectional lift coefficient
C_L	=	wing lift coefficient
C_M	=	wing quarter-chord pitching moment coefficient
C_B	=	wing-root bending moment coefficient
e	=	span efficiency factor
J	=	cost function
B_{WR}	=	wing-root bending moment
N	=	number of discrete vortex elements
p	=	pressure
Re	=	Reynolds number
s	=	semiwidth of vortex pair
S	=	reference area
u^*	=	artificial velocity
u, v, w	=	velocity components in x, y, and z
u_b	=	blockage velocity
V_∞	=	freestream velocity
W	=	weight
W_A	=	wake area
α	=	angle of attack
γ	=	spanload
Γ	=	circulation strength
η	=	normalized semispan
λ	=	Lagrange multiplier or taper ratio
ξ	=	x-component of vorticity
ρ	=	density
ψ	=	stream function

Subscripts

0	=	zero-order
2	=	second-order
e	=	elliptic
g	=	geometric
i	=	index or induced
j	=	index
p	=	profile
ref	=	reference
t	=	total
∞	=	freestream

I. Introduction

The availability of jet fuel is soon to see a decline, accompanied by a projected increase in air traffic within the commercial aviation market.[1] Unfortunately, these two circumstances cannot peacefully coexist. Due to a stagnation in crude oil production, a global initiative to decrease carbon emissions, and the prioritized production of motor gasoline and other petroleum products, jet fuel production cannot increase corresponding to increased aviation industry demand. This is dire news for the American aviation industry, and in turn the American economy. In order to increase air traffic and expand industry, the aviation sector needs to find ways to reduce fuel consumption. One way to accomplish this is to increase the efficiency of the current and future aircraft that are used.

The greenhouse gas emissions created by aircraft contribute to global climate change, which can pose dangerous threats of rising sea levels and flooding. Greenhouse gas emissions by most commercial aircraft include carbon dioxide (CO_2) mono-nitrogen oxides (NO_x), water vapor, and soot particles.[2] Globally, transportation contributes to 14% of man-made greenhouse gas emissions (it is fourth after Electricity and Heat Production, 25%, Agriculture, 24%, and Industry, 21%).[3] Aviation contributes between 2-3% of the global transportation emissions.[2] As the warming effect of all economic sectors on the health of the earth's climate is an immediate and major concern, limiting the emissions by the aviation industry is currently a subject of interest. Especially compelling is that carbon dioxide emissions are a direct result of fuel burn, which is a large portion of the operating cost of any aircraft, and represent inefficiencies in the aircraft design or operation.[2] In order to reduce the amount of emissions of the aviation sector that contribute to climate change, increasing the efficiency of current and future aircraft is absolutely necessary.

Today's aircraft are developed for high efficiency using modern design tools, like multi-disciplinary design optimization (MDO). These design methods correlate the complex interdependencies between aircraft subsystems, such as the aircraft aerodynamics, structural mechanics, and propulsion system. The result of this process is the optimization of a desired design quantity (e.g., minimum cruise drag) for a set of fixed boundary conditions. The most accurate equations that could be used for optimization are typically too computationally complex to solve numerically (optimization is typically done via low-fidelity methods, such as Euler

bending methods for structural considerations and Euler or panel methods for aerodynamic considerations). The high-fidelity method used by Walsh et. all[4] at NASA Langley Research Center took at least 5 hours of wall-clock time to complete one design cycle using parallel computing on 32 processors. Considering they analyzed about 25 different design cycles, the computational time alone would have taken over 5 days, simply to reduce drag from an initial level, not to necessarily find an absolute optimum.[4]

Using a low-fidelity method is significantly less computationally intensive than more robust high-fidelity methods, but they do not provide a full representation of each individual subsystem. For example, panel methods or Euler equations ignore the effects of fluid viscosity when representing the aircraft aerodynamics. Viscosity plays an important role in parasite drag, which contributes to the total drag of the vehicle. For a typical jet transport, the induced drag is only about 33% of the total drag, with 67% of the total drag being parasitic in origin.[5] While a few more recent investigations have included viscous effects in the MDO process, these viscous effects were introduced in simple empirical relationships that lacked a physical interpretation. In order to create a wing design optimized for low drag in real flight conditions, the viscous effects must be understood and appropriately included.

The goal of this study is to understand how to the optimum spanload design changes when incorporating viscous representation, and to experimentally evaluate different theoretical optimums to see how close the theoretical predictions are to the experimental results. Optimized spanwise loadings created under different constraints for both inviscid and viscous formulations were developed to create wing wind tunnel models. The performance of the different wing geometries were studied using a 5-hole probe wake survey measurement technique and force-balance measurements. The results provide a case study to understand the fidelity of these low order methods for aerodynamic design as the project incorporates the structural and viscous effects on wing design. One aspect investigated by this current study is whether a simple correction can be made to the Euler or panel method assumptions to account for viscosity effects, thereby allowing the low-fidelity method to accurately consider viscosity.

II. Background

In an ever present attempt to increase the aerodynamic efficiency of aircraft, the theoretical research into optimizing wings for minimum drag has been a topic of interest in the field of aeronautics. In aerodynamics, the spanwise loading with minimum induced drag for a given lift and fixed span is an elliptical lift distribution after Prandtl[6] and Munk.[7] In circulation theory, this spanload produces a constant vortex-induced downwash across a lifting line. The elliptic spanload has served as a starting point in wing design for nearly a century, but other theoretical optimum solutions have also been developed. These subsequent studies have incorporated multidisciplinary aspects of aircraft design by considering wing structural weight or other aspects of wing design like non-planar wings or wingtip devices. These studies demonstrate that the optimization method can be used with a multitude of constraints, with and without incorporating viscous effects, to find solutions for design problems that are ever more challenging.

II.A. Examples of Optimized Solutions for Induced Drag

In many classical and modern studies on wing design optimization, wing-root bending moment has served as a surrogate term for wing structural weight as the bending moment typically scales directly proportional to wing structural weight. If a wing-root bending moment constraint is used in the place of a span constraint in a wing optimization study, the resulting spanload for minimum induced drag becomes non-elliptical. Jones[8] and Klein and Viswanathan[9] both worked to determine optimized spanloads for this set of constraints. When increasing the span from an elliptic wing, the optimum spanload had significant unloading near the wingtip and a higher loading near the wing root, with the same wing-root bending moment and lift coefficient as the original elliptic wing.

Prandtl[10] also formulated an analytic, optimized solution without the fixed span constraint, but instead utilizing a fixed integrated bending moment and fixed lift constraints. He found an analytic expression, which provided for an optimum solution with characteristics similar to that of Jones[8] and Klein and Viswanathan.[9]

Klein and Viswanathan[11] found an optimized solution for fixed lift and structural weight by assuming that structural weight scaled proportionally with the span-integrated bending moment and shear stress. They found an analytic expression for the optimum spanwise loading which allowed for a 7% decrease in induced drag, for a 16% increase in span, than that of an elliptic

wing with the same structural weight and lift. This spanload had significant unloading near the wingtip, but an equal amount of loading as the elliptical wing near the root. To match the lift, the optimum spanload solution deviates above that of the elliptical solution for non-dimensional span $0 \leq \eta \leq 0.5$.[11]

Löbert[12] investigated trapezoidal forward and aft-swept wings and compared them to an optimized spanload with minimum induced drag with constant wing weight and lift. The weight constraint was implemented by constraining the integrated bending moment per unit sectional thickness. By fixing this integrated bending moment and lift, as well as area, sweep angle and thickness distributions, a unique optimum spanload was found. It was found that the forward-swept wing spanload was extremely similar to this optimum spanload, implying that small amounts of twist would allow its performance to be increased. However, the aft swept wing spanload was more dissimilar from the optimum spanload as it had a lower load at the root hardly any unloading in the outboard portion of the wing. These differences implied that fairly large amounts of twist would need to be incorporated into the trapezoidal wing design in order to match the optimum spanload. Adding this much twist would cause drag penalties in the off-design conditions.[12] The effects of forward and aft sweep in minimizing induced drag was also investigated by McGeer[13] for wings of given structural weight, elasticity, and maximum load factor. In this study, it was found that forward sweep had a theoretical reduction of induced drag at cruise of about 10%, but could have potentially greater reductions for the wings of aircraft like sailplanes, where the wing weight to lift ratio is high.

II.B. Examples of Optimized Solutions for Total Drag

Total drag can also be minimized when searching for an optimum solution. Kroo[14] was able to utilize a strip theory approach in order to incorporate the sectional profile drag coefficient into the optimization problem. In this method the sectional profile drag was represented as a quadratic fit of the drag of an airfoil section with respect to the sectional lift coefficient. In doing so, the sectional pressure drag and skin friction drag contributions to the total drag could be accounted for during the optimization routine.

This method of modeling viscous effects in the optimization process was also used by Verstraeten and Slingerland[15] in order to identify drag characteristics for planar and non-planar wings. The method of Lagrange multipliers was used with a wing-root bending moment constraint in order to optimize and compare wings with the same structural weights. This method

compared viscous and inviscid optimized wings. In this method, profile drag was included for the viscous optimized wings by assuming the profile drag was a function of the local lift coefficient as was done by Kroo.[14] The theoretical results found that the non-planar C wing had no advantages over a wing with winglets. However, the results did indicate that including winglets reduced the drag of the wing by 5.4% when comparing to a planar wing of the same span.

The next step for using these simple viscous corrections in the optimization routine would be to incorporate them into larger design spaces like how Ning and Kroo[16] used this method to incorporate optimum designs of wings and wing tip devices into full aircraft configurations. They found that besides incorporating viscous drag effects, conceptual wing designs also depended heavily on structural considerations like the depth of the wing structural box, the differences in cruise and maneuver loading, and wing skin thickness.

II.C. Multidisciplinary Design Optimization Methods for Drag Reduction

Low-fidelity approaches have allowed a great deal of insight into minimum drag solutions for wing designs. However, modern advancements in computing technology has led towards advancements in the area of drag reduction for more than just wing design, but for full-aircraft configurations using Multidisciplinary Design Optimization (MDO). In utilizing MDO methods, a structural modeling method is typically coupled to an aerodynamic modeling method and an optimization routine. Through the MDO process, a full-aircraft configuration can be produced, which optimally conforms to a given set of design criteria.[17]

Lyu and Martins[18] investigated blended-wing body aircraft optimization, which presented a challenge due to the multidisciplinary nature of the problem. In this study, the authors considered the interdependence on aircraft performance, trim, and stability as well as complexities added by transonic flow conditions and the number of design variables. Using computational fluid dynamics with a Reynolds-averaged Navier-Stokes turbulence model and a method to compute derivatives of aerodynamic forces, they were able to consider a total of 273 design variables when looking for an optimum solution. These design variables included twist, airfoil shape, sweep, chord, and span. The optimization method found a minimum drag for trimmed and stable configurations with fixed lift, trim, static margin, and center plane bending moment constraints. The lowest drag solution was found to be nearly identical to an elliptic spanload.

Another multidisciplinary problem was studied in the work of Antoine and Kroo.[19] They explored developments in aircraft design that could reduce noise and emissions, two very important current topics in aircraft design. This led them to develop a preliminary design tool that could be used to determine optimal aircraft configurations while balancing the relationships between emissions, noise, and cost. A noise prediction code (ANOPP) developed at NASA Langley Research Center, an engine simulator from NASA Glenn Research Center, and aircraft design and optimization tools developed at Stanford University were all incorporated into the tool. The tool could be used to formulate an extremely low emission solution, a decrease in NO_x emissions by 51% for a 9% increase in cost. This type of formulation could dramatically increase the environmental sustainability of the aviation industry. It was also found that aircraft could be designed in order to fly slower at lower altitudes, which allowed for a balance of noise, emissions, and fuel consumption.

MDO methods are oftentimes used for initial aircraft design, which have prohibitively large design spaces and related cost. As such, low-order methods of limited fidelity are often required for these initial design optimization processes as the higher-fidelity simulation techniques are not cost-effective for the early stages of design. Having low-order methods that account for effects experienced by real aircraft like viscosity is therefore incredibly important, as the effects of viscosity play such a large role in many types of real fluid flow.

II.D. Experiment Objectives and Motivation

In the current study, three optimum planar-wing spanloads were used. One was the historical baseline: the elliptic spanload, found by implementing a fixed lift and fixed span constraint for minimum induced drag. In this work, the optimum wing found with these constraints is deemed the "Elliptic Wing." The second optimum spanload was found by relieving the fixed span constraint and instead using a fixed wing-root bending moment constraint, as well as fixed lift, for minimum induced drag. The wing-root bending moment can be used as a surrogate for the wing structural weight, as the two have historically been assumed to scale proportionally. In this work, the optimum wing found with these constraints is deemed the "Inviscid Optimized Wing." The final optimum spanload used in this current study was found, again, by relieving the fixed span constraint and using instead a fixed wing-root bending moment constraint, as well as fixed lift, but now for minimum total drag. The minimization of total drag was performed using a strip

theory approach, where profile drag could be incorporated into the optimization routine. In this work, the optimum wing found with these constraints is deemed the "Viscous Optimized Wing."

The classical studies for minimizing induced and total drag are incredibly useful in understanding how to achieve a spanload that can optimally fit a set of design criteria. However, the fidelity of these classical studies for minimizing induced drag, or total drag under a wing bending-moment constraint, have not been experimentally validated. As viscous effects play a major role in low Reynolds number flow, understanding the efficacy of a simple viscous correction to an otherwise inviscid optimization routine becomes increasingly important in the wing design. Understanding the balance between the fidelity and the expense of this type of low-order method is critically important when deciding how to begin the optimization of a wing or full-aircraft configuration for a given set of design criteria.

The goal of the current study is to experimentally assess the aerodynamic performance of wing geometries that have been optimized using low-order methods, with and without incorporating viscous effects. This assessment was done by first calculating optimum spanloads from a discrete vortex element method with an embedded Trefftz plane analysis routine for three different sets of design criteria. The optimum spanloads were calculated from a discrete vortex element method with an embedded Trefftz plane analysis routine. This design method follows the work of Blackwell[20] and is based upon the fundamental concepts of circulation theory. This analysis resulted in the creation of three separate wing designs which were used for wind tunnel experiments. The measurements of the total wing lift and drag were collected during a series of wind tunnel experiments from force balance measurements. The spanwise lift distribution was also measured using a wake-survey technique. These experimental measurements were then used in order to understand the accuracy of the aerodynamic predictions from the low-order design method with empirical viscous corrections.

II.E. Theoretical Design Methods

The optimum spanloads were calculated by Wroblewski and Ansell.[21] However, for the purposes of a complete understanding of the experimental evaluation detailed in this current work, many relevant details of this previous work will be reproduced here.

II.E.1. Wing Design Criteria

The design criteria used for the optimization routine were chosen in such a way that the three different designs would be as similar as possible so that the comparisons between the wings were

confined solely to the differences between their aerodynamic performance. This approach was used in order to investigate the accuracy of the aerodynamic predictions and design routines for both the inviscid and viscous optimization routines. As such, the wings were all straight tapered wings and had the same area and taper ratio, so the chord distributions were predetermined and the twist distributions for each wing were modified to achieve the desired spanloads. In order to satisfy the design constraints, the lift coefficient, wing-root bending moment, and Reynold's number were all set to be the same. Since the area remained constant but the span varied for each wing, the mean aerodynamic chord of each wing was different. As a result, the experimental freestream Mach of the experiments was varied accordingly in order for each wing to be tested at the prescribed Reynolds number. The twist and aspect ratio of the wings were then tailored to achieve the desired spanload.

All wings were planar and the airfoil was a symmetric NACA 0015 in order to ensure simplicity and valid comparison between the wing models. The geometric and aerodynamic parameters used for all three wings are tabulated in Table II-1. Using non-planar configurations and wing-tip devices, as well as specially designed airfoils can have tremendous benefits in terms of aerodynamic performance, though use of these configurations were outside of the scope of the current study. Instead, the goal of the current study is to compare different optimization methods and constraints.

Table II-1 Aerodynamic and geometric parameters for wing designs

C_L	0.439
$\frac{b}{2} C_B$	0.279
$\mathbf{Re}_{\bar{c}}$	450,000
Airfoil	NACA 0015
Planform Taper Ratio (λ)	0.5
Wing Reference Area (S)	1.385 ft^2

II.E.2. Elliptic Wing Optimization

The optimum spanloads were calculated following the method discussed by Blackwell[20] where aircraft lifting surfaces are represented by a discrete vortex element method. An embedded Trefftz plane analysis routine was used to determine the induced drag of the wing by projecting the induced cross-flow velocity normal to the surface of this plane to the near field, assuming a fixed wake. The induced drag was evaluated using Munk's second theorem, which allows for the computations to be carried out, not in the real plane, but at the Trefftz plane, which simplifies the

calculation.[20] This final step allows for aerodynamic forces and moments to be determined by relating the local bound circulation (Γ_j) of a wing section to the spanload using the Kutta-Joukowski theorem.

$$\frac{\Gamma_j}{V_\infty} = \frac{(C_l c)_j}{2} \tag{II.1}$$

A useful expression is that of the normalized spanload (γ_j). In this expression, c_{avg} is the mean geometric chord of the wing.

$$\gamma_j = \frac{(C_l c)_j}{c_{avg}} \tag{II.2}$$

The Biot-Savart law dictates that the induced velocity normal to a point on the Trefftz plane in the far-field will be twice the value of one in the near-field. This is due to the fact that the velocity in the far-field is induced by a series of infinite vortex lines, whereas the velocity near the lifting line is only affected by semi-infinite vortex lines. The induced velocities at the Trefftz plane can be expressed in terms of the spanload distribution, as the induced velocities produced by the circulation shed into the wake are directly dependent on the spanload. Since circulation and induced velocities can both be expressed in terms of spanload distribution, the expressions for induced drag and lift can be re-written in terms of the wing spanload.

$$C_{D_i} = \sum_{i=1}^{N} \sum_{j=1}^{N} \gamma_i \gamma_j s_i A_{ij} \tag{II.3}$$

$$C_L = 2 \sum_{j=1}^{N} \gamma_j s_j \tag{II.4}$$

In the previous expressions for $C_{D.i}$ and C_L, s_j is the normalized semiwidth of a given vortex pair and A_{ij} is the aerodynamic influence coefficient.

The method of Lagrange multipliers was used in order to determine the spanload that minimizes induced drag under a given design constraint. The method discussed by Kroo[22] was used specifically. This method was designed to calculate spanload distributions for planar and non-planar wings with fixed lift, structural weight, and/or trim constraints. Different cost functions were used for each wing, depending on the design constraints. For the Elliptic Wing, the cost function (J) was used to minimize induced drag of a wing at a fixed lift coefficient.

$$J = C_{D_i} + \lambda_{C_L}(C_L - C_{L_{ref}}) \tag{II.5}$$

When using the method of Lagrange multipliers, the objective is to minimize the cost function. This is done when the partial derivatives with respect to each independent variable of the cost function is equal to zero, indicating an extremum in the analytical solution. Substitution of C_{D_i} and C_L from II.3 and II.4 into the cost function in II.5, allows for a linear system of equations to be formulated (II.6).

$$\begin{bmatrix} \frac{\partial J}{\partial \lambda_j} \\ \frac{\partial J}{\partial \lambda_{C_L}} \end{bmatrix} = [0] \tag{II.6}$$

The equation II.6 can be solved to minimize the cost function and produce the Lagrange multiplier for the lift coefficient constraint (λ_{C_L}) and the optimum spanload which can be seen in Figure II-1 as a function of the normalized semispan (η). Also shown in this figure is the elliptic load of Prandtl[6] for comparison. For this optimum spanload, the calculated span efficiency factor was 1.00, which agrees well with the ideal value of unity.

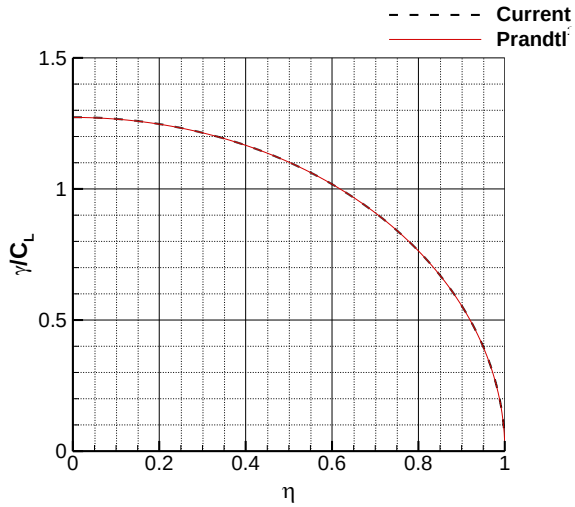

Figure II-1 Elliptic Wing spanload, with comparison to theoretical optimum of Prandtl[6]

II.E.3. Inviscid Wing Optimization

For the Inviscid Wing, the cost function (J) was used to minimize induced drag of a wing at a fixed lift coefficient constraint and a fixed wing-root bending moment constraint. This version of the Lagrange multipliers follows the work of Blackwell[20] and Verstraeten and Slingerland.[15]

$$J = C_{D_i} + \lambda_{C_L}\left(C_L - C_{L_{ref}}\right) + \lambda_{C_B}(C_B - C_{B_{ref}}) \tag{II.7}$$

where

$$C_B = \frac{1}{2}\sum_{j=1}^{N} \gamma_j s_j \left(\frac{2y_j}{b}\right) \tag{II.8}$$

The linear system of equations to be solved in order to produce the optimum spanload becomes:

$$\begin{bmatrix} \dfrac{\partial J}{\partial \lambda_j} \\ \dfrac{\partial J}{\partial \lambda_{C_L}} \\ \dfrac{\partial J}{\partial \lambda_{C_B}} \end{bmatrix} = [0] \tag{II.9}$$

In order to select an optimum span ratio between the Inviscid Optimized Wing and the Elliptic wing, the induced drag ratio of the Inviscid Optimized Wing to the Elliptic Wing ($C_{D_i}/C_{D_{i,e}}$) was plotted against span ratio to find a minimum. This plot is presented in Figure II-2 with the same values as those found by Jones[8] and Klein and Viswanathan[9] for comparison. From Figure II-2, the induced drag ratio for the Inviscid Optimized Wing is consistent with those determined from these classic studies.

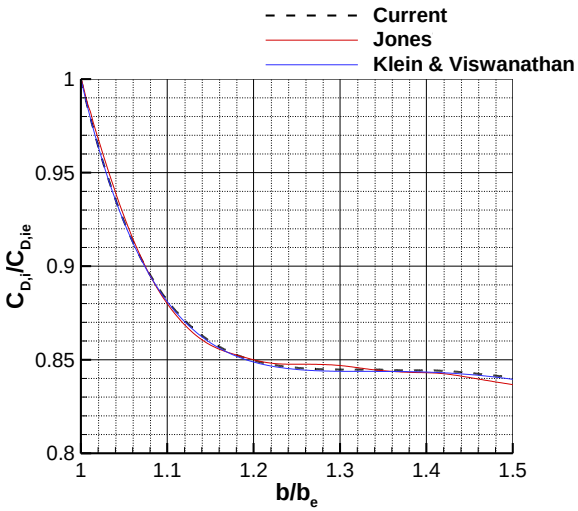

Figure II-2 Ratio of induced drag of optimally-loaded wing relative to elliptically-loaded wing having equal wing-root bending moment and lift.[8,9]

From Figure II-2 it can be seen that the induced drag ratio decreases as the span increases, but since the solution is inviscid, the induced drag of the Inviscid Optimized Wing approaches zero as its span approaches infinity. As a result, there is no true minimum point to select for the optimum span ratio. However, there is an inflection point at $b/b_e = 4/3$ that was selected by Klein and Viswanathan as the optimum span ratio.[9] This inflection point was also used as the optimum span ratio for the current study.

II.E.4. Viscous Wing Optimization

The Viscous Optimized Wing optimum spanload was found by further following the work of Kroo[14] and Verstraeten and Slingerland.[15] This formulation included the influence of the profile drag, allowing the wing design to be optimized by optimizing for the total drag instead of the induced drag. The total drag is found as the sum of the induced drag and the profile drag. The profile drag coefficient ($C_{d,p}$) of a local section of the wing is assumed to vary quadratically with the sectional lift coefficient as seen in II.10.

$$C_{d,p} = C_{d,0} + C_{d,2}C_l^2 \tag{II.10}$$

The local Reynolds number of a non-rectangular wing varies across the span of the wing as the chord varies. The profile drag coefficient depends on Reynolds number, so the variation of the Reynolds number as the chord changes needed to be incorporated into the optimization routine. To do this, $C_{d,0}$ and $C_{d,2}$ were identified for a range of Reynolds numbers within the design space. These coefficients were determined using the XFOIL program developed by Drela and Youngren.[23] This program couples inviscid flow solutions to integral boundary-layer methods allowing for estimates of profile drag of airfoils. In order to calculate the profile drag for the entire wing, a strip theory approach was used. This method incorporates the chord distribution and the airfoil profile drag coefficient. With the profile drag contribution to total drag now able to be calculated, the expression for total drag can be written as:

$$C_D = \sum_{i=1}^{N}\sum_{j=1}^{N}\gamma_i\gamma_j s_i A_{ij} + \sum_{i=1}^{N}\left[C_{d,0_i} + C_{d,2_i}\left(\frac{\gamma c_{avg}}{c}\right)_i^2\right] \tag{II.11}$$

Now with a new expression for total drag, the cost function used to minimize total drag for fixed lift coefficient and fixed wing-root bending moment becomes:

$$J = C_D + \lambda_{C_L}\left(C_L - C_{L_{ref}}\right) + \lambda_{C_B}(C_B - C_{B_{ref}}) \tag{II.12}$$

The Viscous Optimized Wing drag can now be compared to the Elliptic Wing in the same way that the Inviscid Optimized Wing was in the previous section, but instead of comparing induced drag ratios, the total drag ratios are compared. The total drag ratio between the Viscous Optimized Wing and the Elliptic Wing ($C_D/C_{D,e}$), having the same lift and wing-root bending moment, can be seen in Figure II-3. Also in this figure are the optimized wing results from Kroo;[14] however, note that while these results were calculated with the same taper ratio of $\lambda = 0.5$, they were found under fixed weight and trim constraints as opposed to fixed wing-root

bending moment. Additionally, the figure also includes results from Verstraeten and Slingerland,[15] but these were found under an optimization routine with the same design constraints of lift and wing-root bending moment, but a different wing taper ratio than the current study. It is important to note that the total drag ratio will be very sensitive to these differences in constraints as well as the profile drag coefficients used in the process. The profile drag coefficient, and therefore the total drag ratio, are sensitive to changes in chord and Reynolds number. As a result, different wing taper ratios and chord distributions greatly affect the total drag ratio. However, the total drag ratio to span ratio for this current study is consistent with these previous studies.

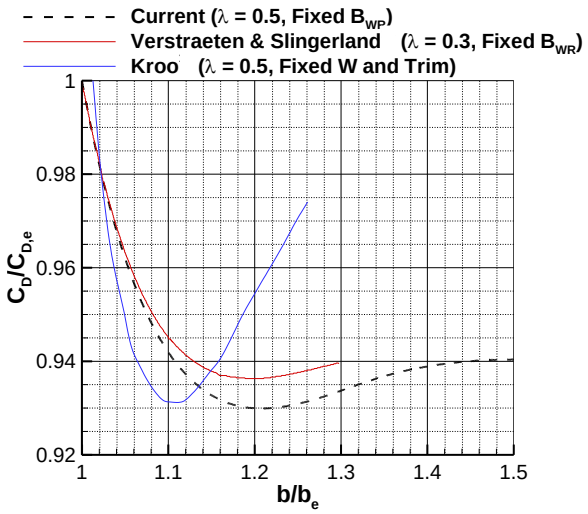

Figure II-3 Ratio of total drag of optimally-loaded wing relative to an elliptically-loaded wing having equal wing-root bending moment and lift.[14,15]

For the current study, based off the results in Figure II-3, the minimum predicted drag of the Viscous Optimized Wing corresponds to a span ratio of $b/b_e = 1.21$.

II.E.5. Wing Design Results

A summary of the resulting drag predictions for the three spanloads at the design C_L and $\frac{b}{2} C_B$ are presented in Table II-2.

Table II-2 Drag predictions produced by optimal spanload configurations.

Spanload	$C_{D,i}$	$C_{D,p}$	C_D	e	AR
Elliptic Wing	0.00942	0.00929	0.01871	1.00	6.5
Inviscid Optimized Wing	0.00796	0.00954	0.01750	0.666	11.6
Viscous Optimized Wing	0.00798	0.00941	0.01739	0.806	9.5

The optimum spanloads that are produced by the three design cases are plotted in Figure II-4 against a normalized span (η).

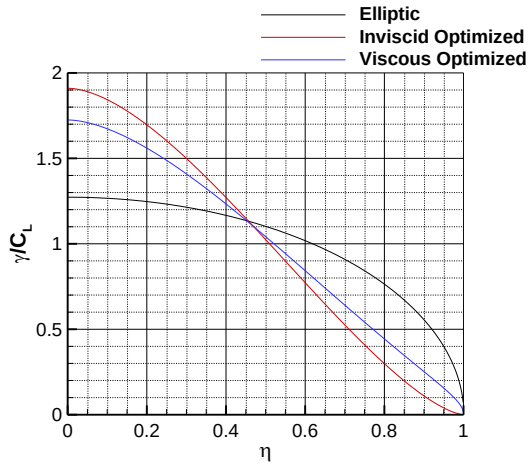

Figure II-4 Spanloads of the optimally-loaded wing designs.

The elliptic wing has an elliptic spanload distribution in order to produce a constant downwash profile across the span, resulting in the minimum induced drag at a given lift and span. However, the Inviscid Optimized Wing has a "bell-shaped" spanload distribution that is consistent with the literature for inviscid optimization with wing-root bending moment constraints.[9] This distribution allows for significant unloading near the wingtip, but higher loading at the root than the other two distributions. As the span of the Inviscid Optimized Wing is longer than that of the Viscous Optimized Wing, it would make sense that the increased span would lead to an increase in profile drag, even with the decrease in induced drag produced by a span extension. As a result, the Viscous Optimized Wing follows a spanload that falls between the Elliptic Wing and Inviscid Optimized Wing spanloads.

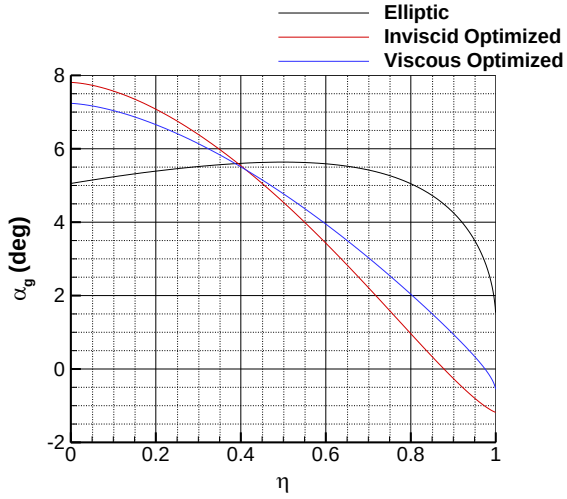

Figure II-5 Twist distributions at design C_L used to achieve design spanload.

As discussed previously, the design spanload was achieved through tailoring the twist distribution, since a prescribed planform configuration was used for all three wings. These resulting twist distributions are given in Figure II-5.

III. Experimental Methods

Three wing models based on the theoretical designs were tested in a wind tunnel at the University of Illinois at Urbana-Champaign. These wing models were used to obtain to force balance measurements, as well as results from 5-hole probe wake survey experiments and surface oil-flow visualization. The methods used for these various experiments are detailed in this section.

III.A. Wind Tunnel

The data obtained in this investigation were acquired from a series of wind tunnel experiments, performed at the University of Illinois at Urbana-Champaign. The Illinois 2.8-ft × 4-ft subsonic wind tunnel located in the Aerodynamics Research Laboratory was used throughout this investigation. The wind tunnel is an open-return, low turbulence, subsonic wind tunnel with a 7.5:1 contraction ratio between the inlet and test section, and turbulence intensity less than 0.1% for all operating speeds and can be seen in Figure III-1.

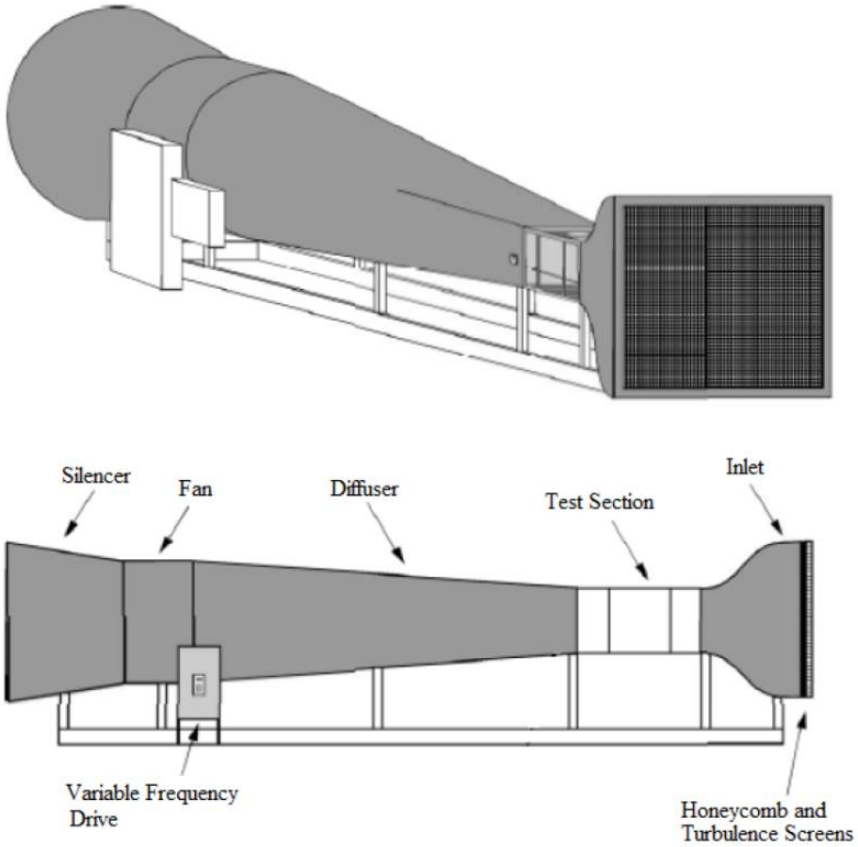

Figure III-1 Wind Tunnel Diagram

The wind tunnel is driven by a 125-hp AC motor connected to a five-bladed fan, which is regulated by an ABB ACS 600 Low Voltage AC Drive. The maximum rotational speed of the fan is 1200 rpm which corresponds to a maximum empty test section speed of 165 mph (242 ft/sec). This results in a maximum tunnel streamwise Reynolds number of approximately 1.5×10^6/ft. The Reynolds number of the wing models were calculated using the mean aerodynamic chord ($\bar{c}$) of each model as well as the tunnel freestream velocity, density, and viscosity as in equation III.1.

$$Re = \frac{\rho V_\infty \bar{c}}{\mu} \tag{III.1}$$

All measurements were acquired at a Reynolds number of 0.45×10^6, based on the wing mean aerodynamic chord. The Reynolds number was kept within 0.5% of the desired value throughout the duration of each experiment. The tunnel test section velocity was calculated using pressure measurements (p) across he inlet and the known areas (S) of the test section (ts) and settling section (ss) of the wind tunnel, as well as ambient conditions inside the laboratory. This calculation was done using a combination of incompressible Bernoulli's equation (III.2), incompressible mass conservation (III.3), and the ideal gas law (III.4).

$$\frac{1}{2}\rho_{amb}V_{ts}^2 + p_{ts} = \frac{1}{2}\rho_{amb}V_{ss}^2 + p_{ss} \tag{III.2}$$

$$S_{ts}V_{ts} = S_{ss}V_{ss} \tag{III.3}$$

$$\rho_{amb} = \frac{p_{amb}}{RT_{amb}} \tag{III.4}$$

Where $p_{amb}$and T_{amb} are the ambient pressure and temperature measurements as R is the ideal gas constant for air. The ambient pressure was measured using a Setra 270 pressure transducer located in the control room and the ambient temperature was measured using a J-type thermocouple.

Using these three equations, the velocity in the test section can be found:

$$V_{ts} = \sqrt{\frac{2(p_{ss} - p_{ts})}{\rho_{amb}\left(1 - \frac{S_{ts}}{S_{ss}}\right)^2}} \tag{III.5}$$

Where $(p_{ss} - p_{ts})$was measured using pressure taps located in the wind tunnel. A total of eight pressure taps were located inside the wind tunnel: four within the settling section on each tunnel

wall, and another four just before the test section on each tunnel wall. Each set of four taps were pneumatically averaged and then connected to a Setra 239 differential pressure transducer.

III.B. Data Acquisition System

The data acquisition programs used for the experiments detailed in this chapter were developed in LabVIEW 2012 and run on a Dell Precision T3400 computer with an Intel® Core™ Quad CPU with 4GB RAM. The computer had a Windows XP 32-bit operating system. The computer software was able to command the various pieces of equipment used for the experiments such as the tunnel variable frequency drive, the three-component force balance, the Zaber traverse system, and the pressure measurement system. Commands were sent by the data acquisition computer to these devices via RS-232 communication. The analog signals from the three-component force balance were converted to digital signals using a National Instruments (A/D) conversion board.

III.C. Force Balance

The model angle of attack was regulated within $0.1°$ using a turntable, which was part of a three-component Aerotech ATE Limited balance located underneath the wind tunnel test section seen in Figure III-2. Measurements acquired from this three-component balance were used to determine the lift, drag, and quarter-chord pitching moment coefficients (C_L, C_D, and C_M, respectively) of the wing models. Load cells were used by the balance in order to measure the forces and moments experienced by the wing models. These load cells could be set to measure loads across a certain range for each component. In order to reduce uncertainty of digitizing the analog measurements, choosing the correct range is important. As each of the three models are relatively small, the lowest range for the load cells was chosen. The normal force range was ± 90 lbf, the axial force range was ± 18 lbf, and the pitching moment range was ± 15 ft-lbf. The load cells output voltage signals, which were low-pass filtered at 1 Hz and then amplified from the original ± 20 mV to ± 5 V using the signal conditioning system within the balance. For each final balance measurement, 200 voltage samples were acquired at a sample rate of 100 Hz and averaged.

Before acquiring force and moment measurements over a range of angle of attack, balance tare voltages were acquired with the wind off. These tare voltages were taken over the entire

range of angle-of-attack range at 1° intervals. These balance tare voltage measurements were subtracted from the balance voltage measurements acquired during the experiment, producing a tare-corrected voltage measurement. This difference in voltage measurements was multiplied by a force balance range ratio (RR) in order to obtain a scaled voltage. For the lowest load cell range, the RR_{normal} was 0.2046, the RR_{axial} was 0.2173, and the RR_{moment} was 0.3413.

The resulting normal force (V_N), axial force (V_A), and pitching-moment (V_M) scaled voltage measurements were put into the calibration matrix (III.6) in order to determine the normal force (F_N), axial force (F_A), and pitching-moment (M).

$$\begin{Bmatrix} F_N \\ F_A \\ M \end{Bmatrix} = \begin{bmatrix} 37.7 & 0.01359 & -0.2095 & 0.01094 & 0 & -0.000865 \\ -0.1607 & 8.3125 & -0.01638 & 0.007084 & 0 & 0.007660 \\ -0.01299 & -0.005521 & 1.247 & -0.002122 & 0 & 0.0001497 \end{bmatrix} \begin{Bmatrix} V_N \\ V_A \\ V_M \\ V_N^2 \\ V_A^2 \\ V_M^2 \end{Bmatrix} \quad \text{(III.6)}$$

These forces can be directly converted into lift, drag, and quarter-chord pitching moment via a coordinate transform.

$$L = F_N \cos(\alpha) - F_A \sin(\alpha) \quad \text{(III.7)}$$

$$D = F_N \sin(\alpha) + F_A \cos(\alpha) \quad \text{(III.8)}$$

$$M_{c/4} = M + x_{offset} F_N + y_{offset} F_A \quad \text{(III.9)}$$

Where x_{offset} and y_{offset} are the distances between the quarter-chord position to the center of the force balance. Since the quarter-chord of the models were mounted directly to the center of the balance plate, x_{offset} and y_{offset} were both zero for the current study.

In order to calculate the non-dimensional lift coefficient (C_L) and drag coefficient (C_D), the lift and drag forces needed to be divided by the freestream dynamic pressure (q_∞) and model reference area (S).

$$C_L = \frac{L}{q_\infty S} \quad \text{(III.10)}$$

$$C_D = \frac{D}{q_\infty S} \quad \text{(III.11)}$$

In order to calculate the non-dimensional quarter-chord pitching moment coefficient (C_M), the pitching moment needed to be divided by the freestream dynamic pressure, model reference area, and mean aerodynamic chord.

$$C_M = \frac{M_{c/4}}{q_\infty S \bar{c}} \tag{III.12}$$

Where the freestream dynamic pressure was calculated using the previously-measured values of ρ_{amb} and U_{ts}

$$q_\infty = \frac{1}{2}\rho_{amb} V_{ts}^2 = \frac{p_{ss} - p_{ts}}{1 - \left(\frac{S_{ts}}{S_{ss}}\right)^2} \tag{III.13}$$

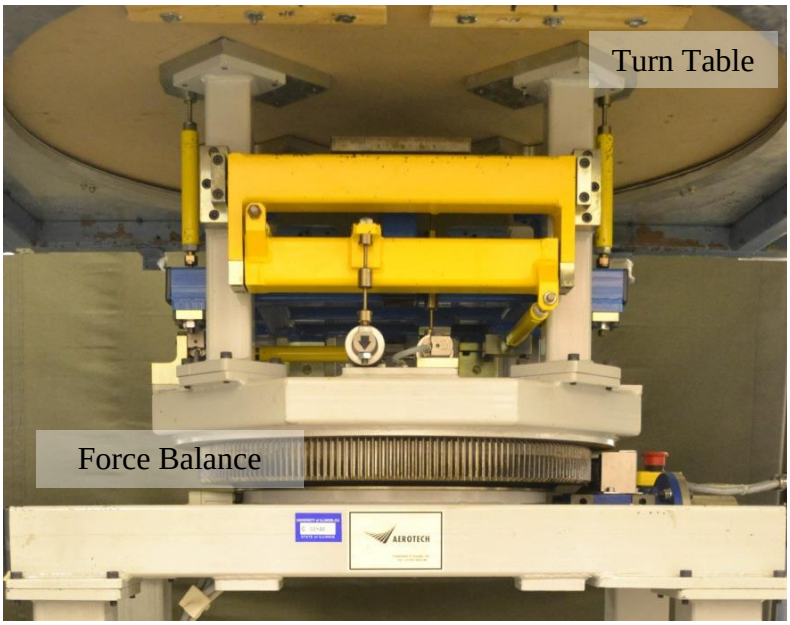

Figure III-2 Photograph of Force Balance

III.D. Wind Tunnel Corrections

Tunnel wall corrections for a 3D wing model were made to these measurements in order to account for solid blockage, wake blockage, streamline curvature, and wall-induced upwash using standard methods described by Barlow et al.[24]

All of the corrections that will be discussed were implemented automatically by a LabVIEW data reduction immediately following the acquisition of all measurements. There are two main factors necessitating corrections factors: the presence of the wing model, which affects the dynamic pressure, and the presence of the tunnel walls, which affects the upwash distributions along both the chord and span of the model.

Blockage correction is necessary as blockage in the wind tunnel induces an incremental velocity increase at the model that changes the dynamic pressure. The forces and moments

experienced by the model scale directly with the dynamic pressure at the model, because the solid model reduces the area of the test section, leading to an artificial increase in dynamic pressure. The solid blockage factor is discussed in Barlow et al.[24] and is given in equation III.12.

$$\epsilon_{sb} = \frac{\Delta V}{V_\infty} = \frac{0.9(Wing\ Volume)}{S_{ts}^{3/2}} \tag{III.12}$$

The wake blockage correction includes the effects of flow separation and more effectively corrects for reductions in velocity across the wake that lead to artificial increases in the dynamic pressure of the freestream. The wake blockage correction is also discussed in Barlow et al.[24] It includes $C_{Du,}$ the uncorrected drag coefficient, $C_{Di,}$ the uncorrected drag due to lift, and C_{Do}, the uncorrected minimum drag coefficient. The equation for wake blockage correction is given in equation III.13.

$$\epsilon_{wb} = \frac{S}{4S_{ts}} C_{Do} + \frac{5S}{4S_{ts}} (C_{Du} - C_{Di} - C_{Do}) \tag{III.13}$$

The second term the drag coefficient due to any separated flow. When there is no separated flow, this term is zero, so equation III.13 gives the wake blockage correction for streamlined flow. The derivation of these terms is described in detail in Barlow et al.[24]

The corrected dynamic pressure is then found as follows:

$$q_{\infty_c} = q_\infty (1 + \epsilon_{sb} + \epsilon_{wb})^2 \tag{III.14}$$

The streamline curvature correction is necessary because the presence of the tunnel walls changes the upwash distribution along the chord of the model. This upwash affects the angle of the attack and pitching moment coefficient of the wing. The streamline curvature correction is a function of the tunnel aspect ratio as well as the ratio of the model quarter-MAC to the width of the tunnel. This correction factor is τ_2 and is automatically found by the data acquisition program in LabVIEW using charts from Barlow et al.[24]

The wall-induced upwash correction factor δ is a function of the spanload distribution, ratio of model span to the width of the tunnel, the shape of the test section, and the position of the wing. The correction factor is determined by finding the effective vortex span of a wing, which is a function of taper ratio and span. The upwash correction factor is automatically found by the data acquisition program in LabVIEW using digitized charts from Barlow et al.[24] and user-input data about the geometry of the model.

The correction factors are applied utilizing the following equations derived in Barlow et al.[24] to find the corrected drag coefficient (C_{Dc}), the corrected angle of attack (α_c), and the corrected quarter-chord pitching moment (C_{Mc}).

$$C_{Dc} = \frac{D}{q_{\infty_c} S} + \frac{\delta S}{A_{ts}} C_{Lc}^2 \tag{III.15}$$

$$\alpha_c = \alpha_g + \frac{\delta S}{A_{ts}} \frac{180}{\pi} (1 + \tau_2) C_{Lc} \tag{III.16}$$

$$C_{Mc} = \frac{M}{q_{\infty_c} S \bar{c}} + 0.125 \, \delta \, \tau_2 \, \frac{S}{A_{ts}} \, C_{Lc} \left(\frac{dC_{Lc}}{d\alpha_{c_{(\text{rad})}}} \right) \tag{III.17}$$

Where α_g is the geometric angle of attack and C_{Lc} is simply found by dividing C_L by $(1 + \epsilon_{sb} + \epsilon_{wb})^2$.

III.E. Construction of Wing Models

Three wing models were constructed according to the designs discussed in section II. The theoretical design defined wings with set taper ratios, surface areas, and spans, as well as chord and twist distributions. CAD models were created in Creo Parametric using NACA0015 airfoil sections and can be seen in Figure III-3. The airfoil sections were placed at small intervals along the span of each wing, and then the wing shapes were created by connecting all of the sections with a swept blend. The sections were spaced closer together in areas where the twist distribution changed rapidly in order to ensure that the model had conformed to specified twist distribution at all points.

Each model was machined from solid aluminum using a 5-axis CNC mill. The aluminum models were then processed through an acid wash and a 1/64-inch thick fiberglass cloth was adhered to the surface. The model surfaces were polished and painted with primer, producing smooth, high-quality surfaces. Photographs of the three wing models installed in the wind tunnel test section are presented in Figure III-4.

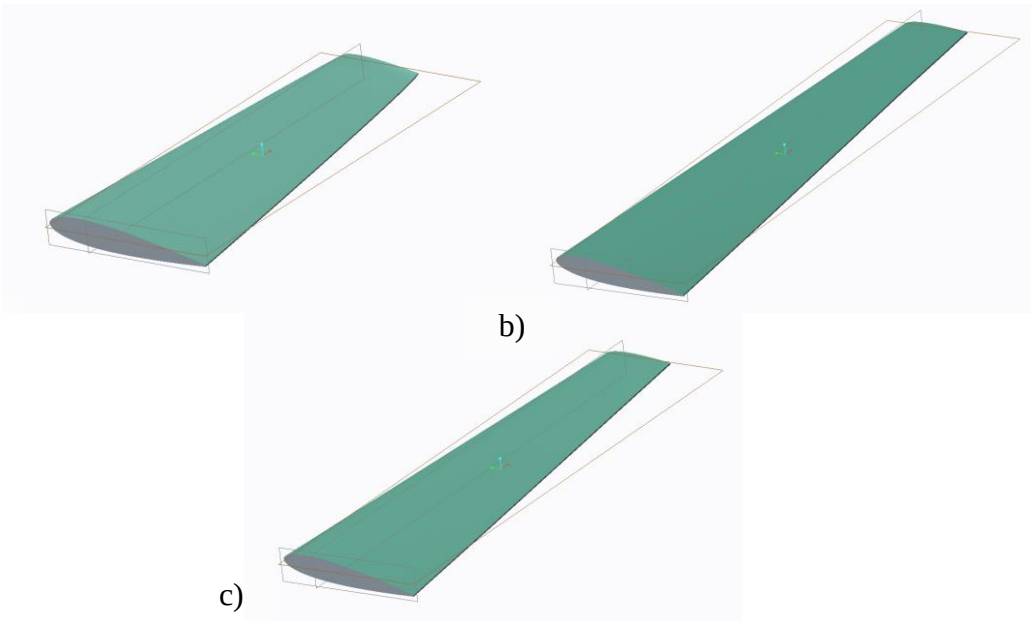

Figure III-3 Isometric view of CAD models for a) Elliptic Wing, b) Inviscid Optimized Wing, c) Viscous Optimized Wing.

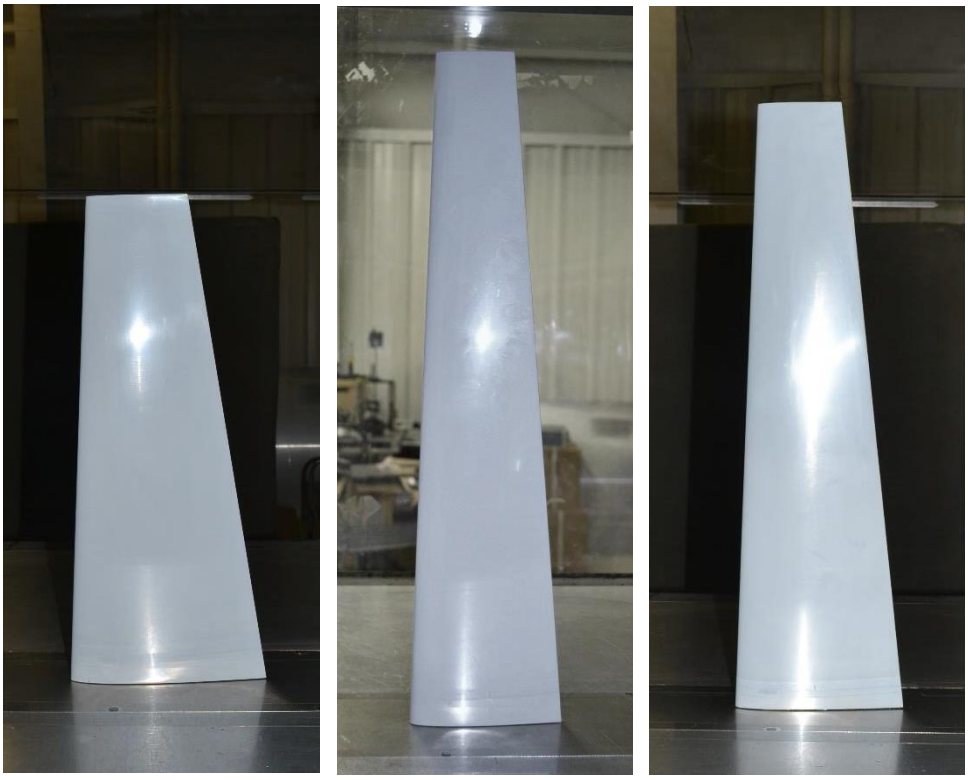

Figure III-4 Wing models installed in wind-tunnel test section: a) Elliptic Wing, b) Inviscid Optimized Wing, c) Viscous Optimized Wing.

III.F. Pressure Measurement System

In order to use the 5-hole probe wake survey method that is detailed in section III.E, pressure data were acquired across a wake-survey plane behind the wing models. The pressure measurements were acquired using an Aeroprobe Corp. model PS5-C318-152 five-hole probe with a base diameter of 0.125 inches. This pressure probe has one central port and four equidistant peripheral ports around the conical tip of the probe. The pressure measurements were acquired using a DTC Initium System manufactured by Pressure System. The DTC Initium collected data from one $\pm$ 0.35 psid Miniature Electronically Scanned Pressure (ESP) 32-port module. This ESP module was connected to the five output pneumatic ports from the five-hole pressure probe, as well as a reference port connected to the tunnel test section static pressure. The tunnel settling section static pressure was connected to port 32. The module was able to measure the pressure difference between each of 6 ports used and the reference port. A schematic of the Pressure Measurement System can be seen in Figure III-5.

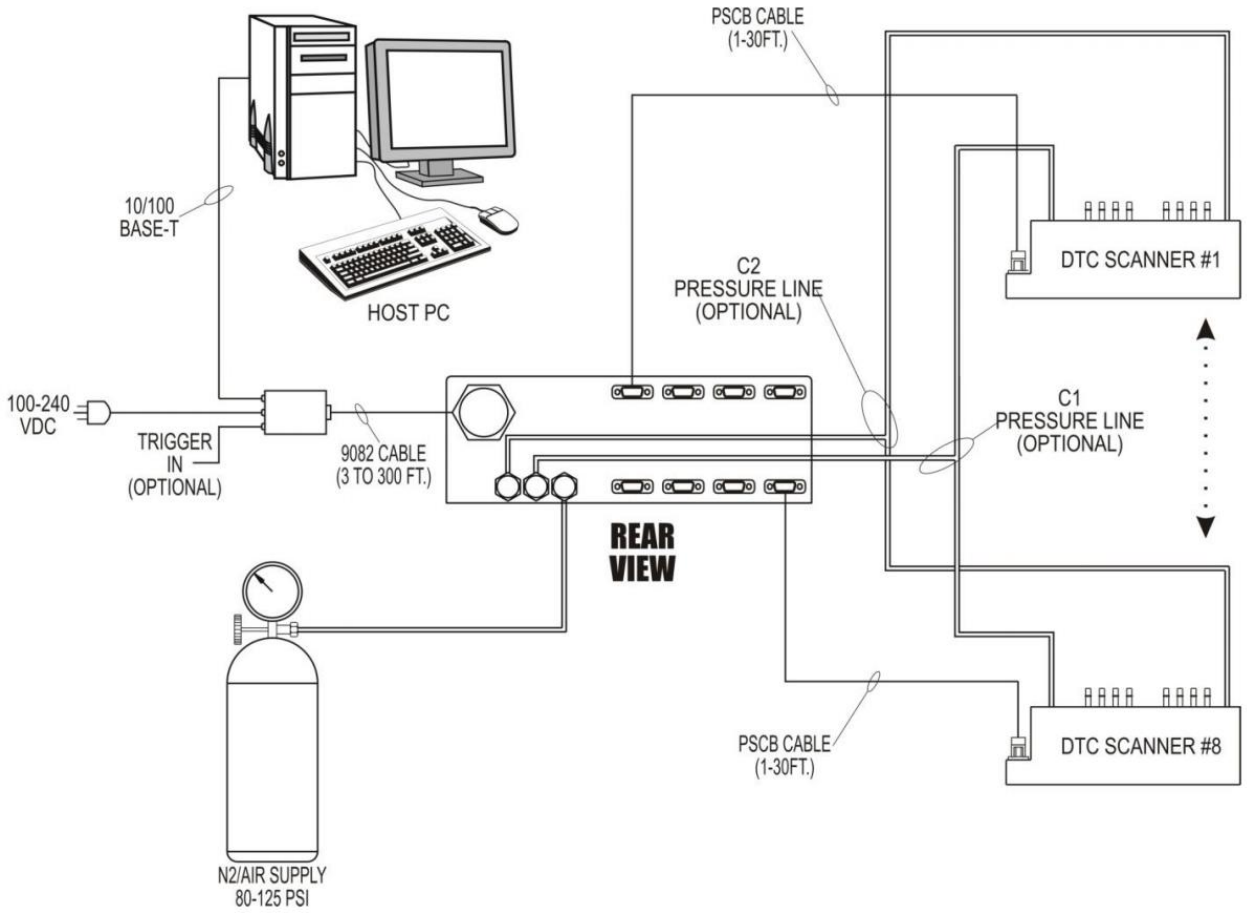

Figure III-5 Schematic of the Pressure Measurement System.

The DTC Initium was connected to the ESP module using a PSCB cable. The Initium was connected to the Dell computer using a 10/100 Base – T Ethernet cable as seen in Figure III-5. Also seen in this figure is the connection between the Initium and a supply of compressed nitrogen gas. The DTC Initium system re-zeroes the ESP module by applying 100 psi of compressed nitrogen through a C1 port on each scanner. This shifts a manifold within the module, which is then shifted back by applying 100 psi of pressure to the port C2. Once this calibration is completed, the pressure measurement system is ready for data acquisition. Vinyl tubing was used to connect the five-hole probe pressure ports and static pressure lines to the ESP module.

III.G. Wake Survey System

A 2-axis traverse system was used to move the 5-hople probe across the wake survey plane. Zaber linear traverses were used for each axis. In the horizontal axis, the Zaber traverse was model A-LST1250BE01-ENG1561-KT07, and in the vertical axis the model was A-LST1000A-E01-KT07. The positions of each traverse were able to be measured with Rotary quadrature encoders within 9.84 thousandths of an inch. Two-phase stepper motors controlled the position of the axes and were connected to the data acquisition computer with an RS-232 cable.

The wake-survey measurement plane is approximately 25 inches behind the quarter-chord location, which is the same for all three models. The experimental setup for the wake-survey method can be seen in Figure III-6. The measurement points selected in the wake-survey plane were entirely dependent on the test conditions, as model produced a different wake at each angle of attack, therefore the position and size of the wake-survey data acquisition grid changed depending on the test in order to capture the entirety of the wake. In order to determine where to collect data, a preliminary wake survey was run for approximately 15 minutes using a 1 in. sampling grid to acquire pressure measurements. The raw pressure data could be viewed using a MATLAB code that plotted the grid of pressures from a selected port. This visualization of raw data was then used to determine the size and shape of a much finer sampling grid in a separate MATLAB code. The finest sampling grid utilized is equal to that of the five-hole pressure probe’s base diameter: 0.125 in. This process was used in order to save time, as acquiring data in such a fine grid is costly. In order to simplify the data reduction process, full rectangular grids of data points were collected. For the portions of the wake-plane where there were no significant

flow features, a coarser grid of 0.25 in. was used. At this resolution, a typical survey at one angle of attack took approximately 9-10 hours, but depended heavily on the span of each model and the size of the wing tip vortex present in the wake.

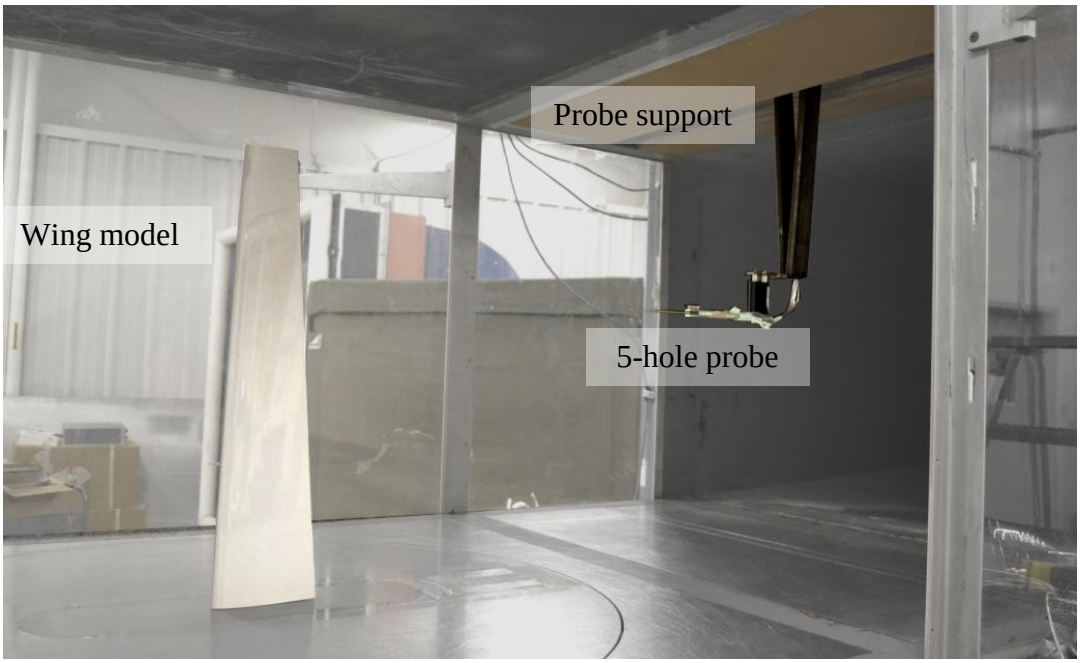

Figure III-6 Photograph depicting the installed wing model, 5-hole probe, and probe support.

The 5-hole probe pressure measurements collected at the wake survey plane were then used in order to calculate the three-components of velocity at the downstream wake survey plane from the wing models. A calibration was required to reduce the raw pressure measurements into the three velocity components. A detailed discussion of the calibration procedure is detailed in Appendix B. The process for converting these velocity measurements is discussed in Appendix C. These measurements were used to determine the spanwise lift, induced drag, and profile drag distributions, as discussed by Brune.[25] This method utilizes the control volume analysis techniques, originally developed by Maskell[26] and Betz[27]. A brief introduction to the wake-survey method is given in this section, but a more detailed derivation can be seen in Appendix A. Wake survey measurements were taken for each of the three wings at four angles of attack. From these velocity components, the vorticity (ξ) and stream function (ψ) terms were first calculated. With these necessary terms, the wake survey technique developed by Brune[25] allows the wing lift (L), induced drag (D_i), and profile drag (D_p) to be calculated from the change in momentum across a control volume surrounding the model.

$$D_p = \iint_{W_A} \left[(p_{t,\infty} - p_t) + \frac{\rho}{2}(u^* - u)\{u^* + u - 2(V_\infty + u_b)\} \right] dydz \tag{III.18}$$

$$D_i = \frac{\rho}{2} \iint_{W_A} \psi \xi dydz \tag{III.19}$$

$$L = \rho \iint_{W_A} y \xi dydz \tag{III.20}$$

In the profile drag equation, u_b is the wake-blockage velocity introduced by Maskell, which takes the form of an x-directional perturbation velocity as an integral over the wake survey area.[26]

$$u_b = \frac{1}{2S_{Tunnel}} \iint_{W_A} \left(u^* - u \right) dydz \tag{III.21}$$

Betz introduced u^*, an artificial velocity component that is different from u in the wake area alone.[27] As such, the difference between u and u^* is zero everywhere except for in the wake of the model. The equation for the artificial velocity can be expressed as,

$$p_{t,\infty} = p_t + \frac{\rho}{2}(u^{*2} + v^2 + w^2) \tag{III.22}$$

The lift in equation III.20 is found using Maskell's method, however Kusunose puts forth a method for determining lift using classical circulation theory with a planar wake assumption shown in equation III.23.[31] This method is extremely useful as it allows for the calculation of sectional lift coefficient using equation III.24.

$$L = \rho V_\infty \int_{y_L}^{y_R} \Gamma(y) dy \tag{III.23}$$

$$C_l(y) = \frac{2}{V_\infty c(y)} \Gamma(y) \tag{III.24}$$

Since ψ and ξ are both functions of the wake velocities, the lift and drag components of the wing can be determined by the 5-hole pressure measurements acquired across the wake plane. The streamwise vorticity calculation requires taking the curl of the cross-flow velocity components across the wake plane,

$$\xi = \frac{\partial w}{\partial y} - \frac{\partial v}{\partial z} \tag{III.25}$$

The stream function is used for the calculation of induced drag and can be found using the *x*-vorticity component. An iterative procedure was used to solve the discrete Poisson equation in order to obtain ψ.[27]

$$\frac{\partial^2 \psi}{\partial y^2} + \frac{\partial^2 \psi}{\partial z^2} = -\xi \tag{III.26}$$

The data reduction also included Savitzky-Golay filtering on the velocity and total pressure distributions before finite difference techniques were used to compute vorticity and the *y*- and *z*-derivatives of the total pressure difference from the freestream value. This filtering helped mitigate the effects of instrument-induced error on the calculation of the derivatives by ensuring a smooth spatial distribution of the velocity and pressure contours. The total pressure difference was defined as $1 - C_{p,t}$ and was calculated using the total pressure measured by the 5-hole probe. The *z*-derivative of the total pressure difference was also used in order to find the position of the wake, so that measurements outside of the wake could be neglected in the calculation of lift and drag components; this includes the portion of the flowfield dominated by a wing-floor juncture vortex. The data reduction is elaborated upon further in Appendix C.

III.H. Oil-Flow Visualization

Fluorescent oil surface-flow visualization was also used in order to identify separation bubbles and other flow features of interest. When performing this qualitative experimental method, the shear forces experienced at the surface of the wing model during tunnel operation cause oil on the surface of the model to move and create a time averaged pattern of the surface flow. In order to perform surface oil-flow visualization, the wing model was first wrapped in black Con-Tact paper, which provided a high-contrast surface for the fluorescent oil image. A thin coat of 10W-30 motor oil was applied to the wing model, and a mixture of Dye-Lite fluorescent leak detector dye and heavy viscosity mineral oil was applied to the wing model using an airbrush. The airbrush used Nitrogen gas regulated at 35 psi in order to apply florescent oil in a very fine speckle pattern. The wing model was rotated to the desired angle of attack and the wind tunnel was run at the desired Reynolds number for approximately three minutes. Black lights were used to excite the fluorescent dye in the oil, and all other sources of light were eliminated. The resulting flow patterns were documented using a Nikon D3100 digital camera with long exposure settings. Flow visualization was conducted for each wing at the design lift coefficient.

IV. Results and Discussion

IV.A. Wing Performance

The resulting performance measurements for the three wing models are presented in Figure IV-1 and Figure IV-2. Since airfoil and wing performance measurements are known to be sensitive to hysteresis effects at low Reynolds numbers, performance data were acquired for both increasing and decreasing angles of attack. The design predictions of C_L and C_D are also provided in Figure IV-1 and Figure IV-2 as filled symbols. The root angle of attack is used as the reference incidence setting for the wing. The interpolated drag coefficient and root angle of attack from the wind-tunnel measurements are also presented in Table IV-1 for each of the three wings at the design C_L. From Figure IV-1 b), since the root angle is different for each wing, the zero-lift α_{root} is also expected to be different for each model. Additionally, within the linear lift regime it can be seen that there is an increase in lift curve slope with increasing aspect ratio. The Elliptic Wing has the shallowest lift curve slope and the Inviscid Optimized Wing has the steepest. From Figure IV-1 a), the predicted behavior in the wing drag is also exhibited, where the drag of the Elliptic Wing has the highest total drag coefficient of the three wing geometries for the design C_L. Also from Figure IV-1 a), the Viscous Optimized Wing produces the smallest drag coefficient at the design C_L. These observations are consistent with the design predictions, as shown in Table IV-1.

Examination of the drag polar reveals that the Inviscid Optimized Wing, having the longest span, has lower drag than the Viscous Optimized Wing and the Elliptic Wing at high lift coefficients. Since the Inviscid Optimized Wing has the largest aspect ratio of all three wing designs, significantly less induced drag is produced by this wing at high values of C_L, despite the lower planform efficiency factor associated with this wing. From Figure IV-1, the Elliptic Wing also exhibits the lowest drag coefficient at $C_L = 0$ of the three wings, followed by the Viscous Optimized Wing and the Inviscid Optimized Wing. As shown in Table IV-1, the Elliptic Wing was designed with the lowest profile drag of all of the three wing designs. Since the wings are operating at an angle of attack that is different from that of the design conditions, it can be expected that a small amount of induced drag is being produced at $C_L = 0$ due to small positive and negative local lift contributions across the span produced in the off-design spanload. However, it is safe to assume that this induced drag contribution is small for this case, and the

trends observed in the drag polar for C_L = 0 are primarily due to the differences in profile drag between the three wing designs.

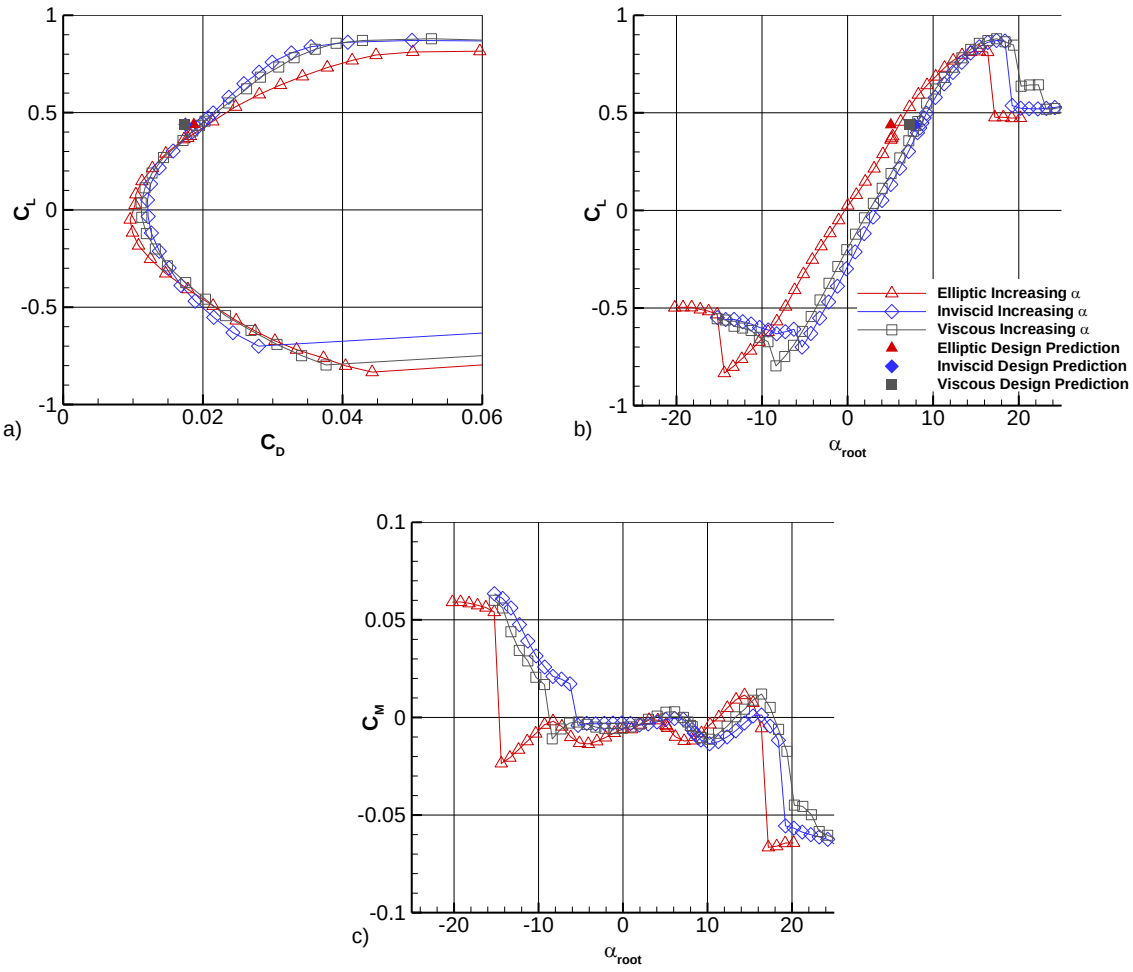

Figure IV-1 Aerodynamic performance of design wing models at $Re\bar{c}$ = 0.45 × 106 for increasing α_{root}: a) CD, b) CL, c) CM.

While the trends in the drag coefficient of the wings agree with the predictions, the exact values of C_L and C_D predicted in the wing designs are slightly different than those acquired from the experimental measurements. This observation is similar to those of Coder and Maughmer[28] for airfoils at low Reynolds numbers, where the theoretic methods tended to over-predict the lift coefficient and under-predict the drag coefficient at a given α, when compared to the experimental measurements. While this slight difference could be due to several factors, the authors attribute a large portion of this discrepancy to the presence of the wind-tunnel floor boundary layer and wing-floor juncture vortex in the wind-tunnel measurements, which was not included in the wing design predictions.

The quarter-chord pitching moment coefficient in Figure IV-1 c) also displays a behavior similar to that of an NACA 0015 airfoil, though one significant difference is the negative pitching moment observed at α_{root} = 0 deg. For the NACA 0015 airfoil one would expect C_M = 0 at α = 0 deg. Though, in Figure IV-1 c) a negative pitching moment is produced for the wings due to the aggressive washout near the tips of each design. From Figure IV-1 and Figure IV-2, the wing performance corresponding to an increasing angle of attack is consistent with that obtained for a decreasing angle of attack, with the exception of the angle-of-attack range near stall.

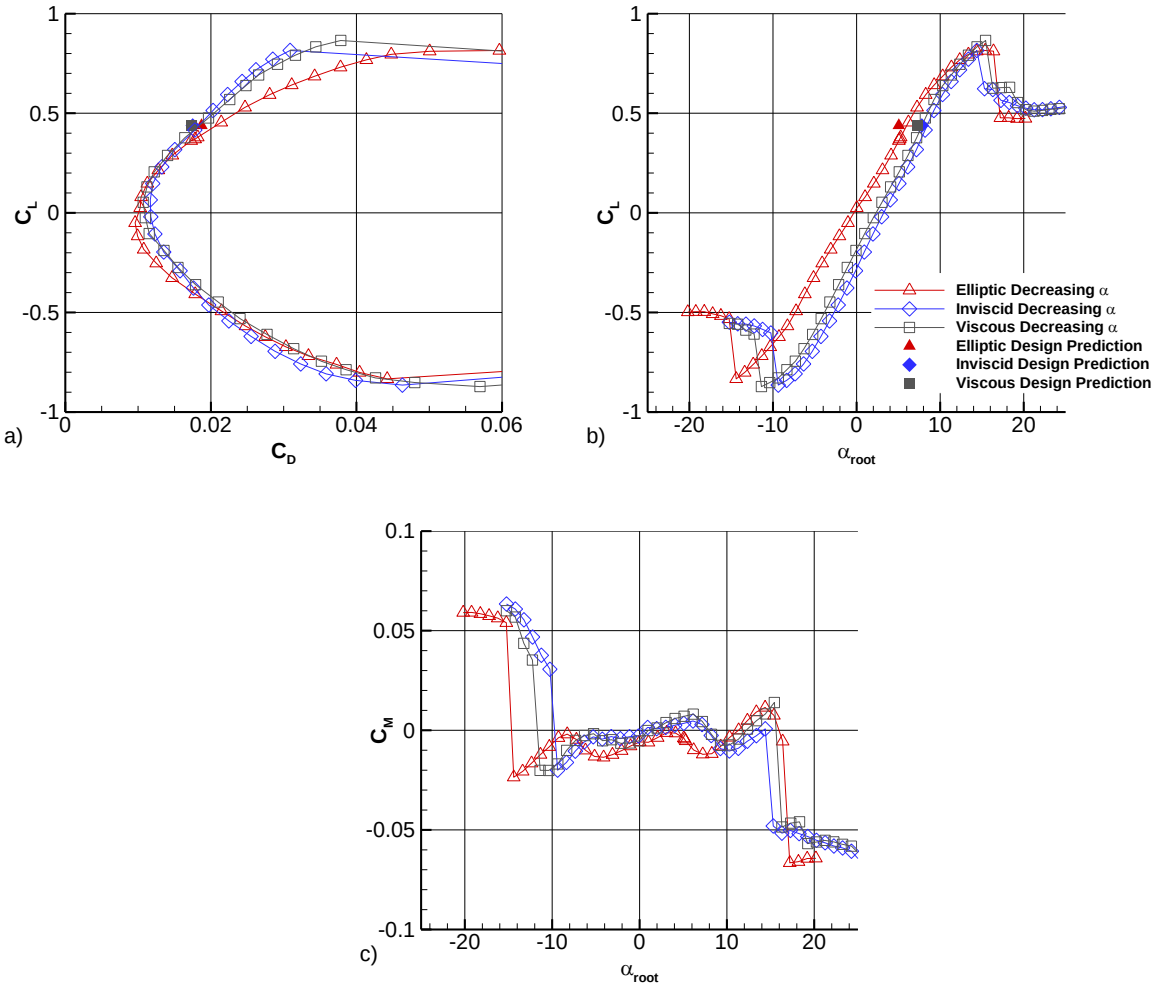

Figure IV-2 Aerodynamic performance of design wing models at Rec^{-} = 0.45 × 106 for decreasing α_{root}: a) CD, b) CL, c) CM.

Table IV-1 Drag and Angle of Attack for Each Wing at Design C_L = 0.439

Spanload	C_D	α_{root} (deg)
Elliptic Wing	0.02158	5.76
Inviscid Optimized Wing	0.01967	8.54
Viscous Optimized Wing	0.01879	7.77

IV.B. Surface Oil-Flow Visualization

The surface-oil flow visualization results for the three wings at the design lift coefficient are also presented in Figure IV-3.

Figure IV-3 Surface-oil flow visualization of wing models at design CL: a) Elliptic Wing, b) Inviscid Optimized Wing, c) Viscous Optimized Wing.

From Figure IV-3, the flow visualization reveals the presence of a separation bubble on each wing. The location and size of the separation bubble was observed to vary across the span of the wing, due to the spanwise twist distribution that was incorporated into the wing designs. Since the local angle of attack across the outboard sections of the wings were lower than those across

the inboard section of the wings, the local flow qualities and separation bubble geometry was observed to vary relative to this twist geometry. A slight influence of the tip vortex can also be observed in each of the flow visualization results, though across the majority of the span the flow appears to exhibit very little spanwise interaction, as indicated by the streamwise flow pattern upstream and downstream of the separation bubble.

IV.C. Wake-Survey

Wake-survey data was acquired for the three different wing models at the design lift coefficient (C_L = 0.439) at $Re_{\bar{c}} = 0.45 \times 10^6$. Contours for the *u*-velocity measurements, the *x*-vorticity component, and the change in total pressure are shown in Figure IV-4-Figure IV-6, since these measurements are important for the calculations of total lift and drag. Vorticity is used for calculating lift and induced drag, and the change in total pressure and the *u*-velocity component are used in the calculation of profile drag. Since each model was run at a different M_∞ to produce a constant $Re_{\bar{c}} = 0.45 \times 10^6$, the dimensional contour levels are different for each wing. It should be mentioned that the vorticity contour for the elliptic wing in Figure IV-4 b) has a different contour scaling than the other wings due to the distinctly high vorticity associated with the tip vortex for this case.

In Figure IV-4-Figure IV-6, the velocity deficit due to the model is clearly visible as the vertically-oriented region of high change in total pressure ($1\text{-}C_{p,t}$). The floor boundary layer and juncture flow adjacent to the model is also clearly visible in the *u*-velocity measurements as the region of low pressure spanning the bottom of the plot for each wing model. The large spanwise twist required to achieve the spanloads of the Inviscid Optimized Wing and the Viscous Optimized Wing also produce a deflection of the wake trace, which can be observed in Figure IV-5 and Figure IV-6. Finally, the tip vortex, resulting from the roll-up of the wake, is also visible for each wing model, but most clearly for the Elliptic Wing in Figure IV-4. In comparing the vortex size between the three wings, the Elliptic Wing has a much larger tip vortex than the Viscous and Inviscid Optimized Wings. This difference in vortex size was attributed to the difference in the spanload configurations local to the tip. The Elliptic Wing, for example, has a much more aggressive decrease in the bound circulation local to the tip than the Viscous and Inviscid Optimized wings do. Since this decrease in bound circulation across the span is fed into the strength of the trailing vortex sheet, it can be expected that the trailing circulation local to the

tip of the Elliptic Wing is significantly stronger than the Viscous and Inviscid Optimized Wings. This increased strength of the vortex sheet leads to a stronger interaction of the free wake, causing a more aggressive roll-up at the tips for this wing configuration. Knowing that increasing aspect ratio decreases induced drag coefficient, it also follows that the longer span, and therefore largest aspect ratio, produces the smaller trailing vortices.

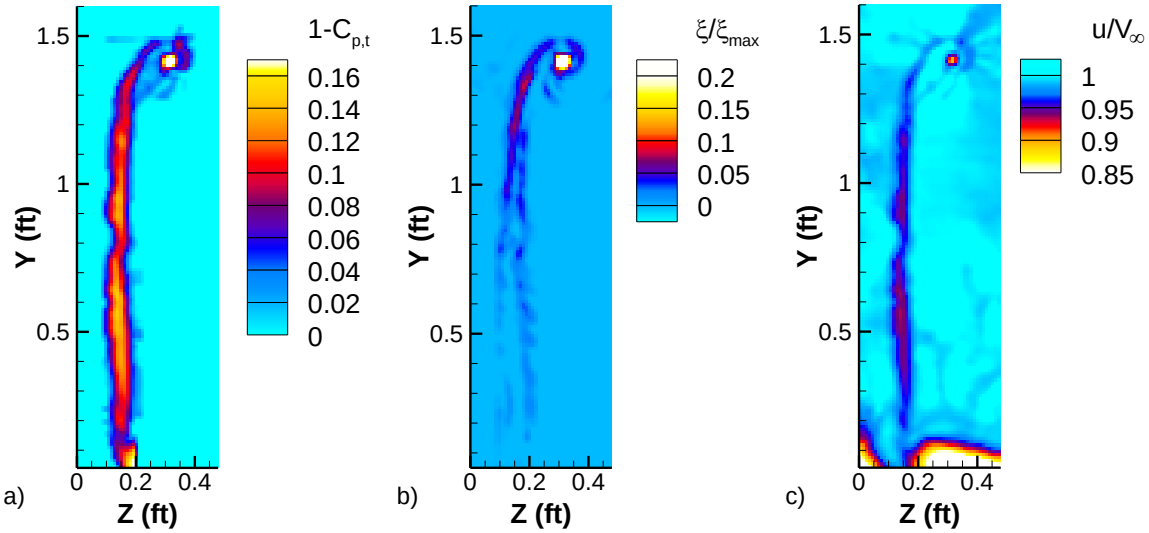

Figure IV-4 Contour plots for the Elliptic Wing for a) 1-$C_{p,t}$, b) ξ, and c) u.

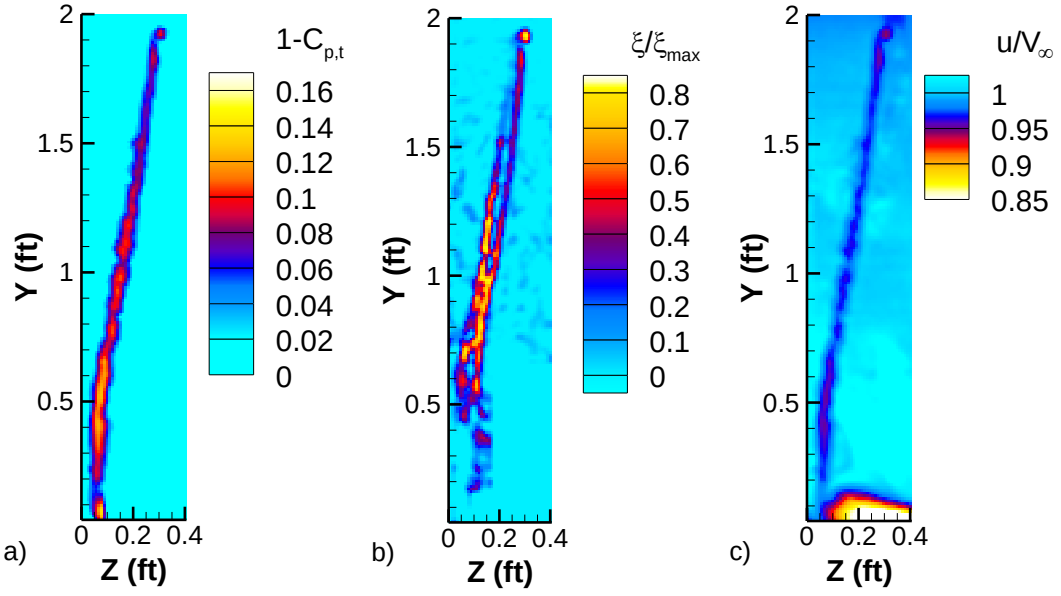

Figure IV-5 Contour plots for the Inviscid Optimized Wing for a) 1-$C_{p,t}$, b) ξ, and c) u.

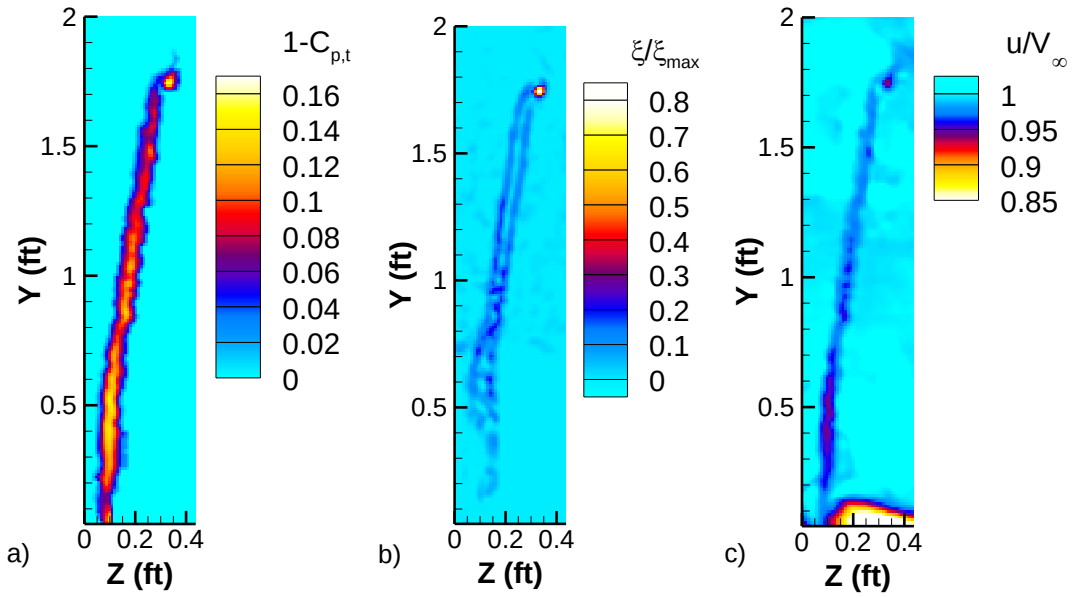

Figure IV-6 Contour plots for the Viscous Optimized Wing for a) 1-$C_{p,t}$, b) ξ, and c) u.

In observing a) for each of Figure IV-4-Figure IV-6, it should be noted that the total pressure difference from the floor vortex generated during wind tunnel testing has been excluded from the measurements, as mentioned in the Experimental Methods section. As a result, the portion of wake area with the floor vortex has been neglected from profile drag calculations. The u-velocity outside of the wake has also been set to u^*, the artificial axial velocity component, so that when profile drag is calculated from Equation III.18, the (u^*- u) term is considered only within the wake. As such, the floor vortex is still visible in the plot of the u-velocity, as it exists within u^*, but it does not affect the calculation of profile drag. This procedure was utilized in order to prevent small amounts of measurement noise or uncertainty from biasing the calculated lift or drag values from the wake survey technique, when integrations were performed across the entire wake plane. From b) for each of Figure IV-4-Figure IV-6, it can also be seen that there is a distortion of the vorticity due to the vortex created at the root of the wing and the tunnel floor, and that this portion of the vorticity is not able to be fully resolved. The floor juncture vortex creates an area of negative vorticity that reduces the calculated lift and induced drag near the root. To combat this effect, negative vorticity near the wing root has been set to zero. Additionally, in Figure IV-4-Figure IV-6 b), it can be seen that the vorticity near the tip has been transported inboard from the tip of the wing due to the wake roll-up. For example, the span of the

Elliptic Wing is 1.5 ft, but in Figure IV-4 b) the maximum vorticity is located 1.417 ft from the root.

The balance polar data is also compared to the wake survey results and design predictions in Figure IV-7-Figure IV-9. In these figures, the axes of the C_L vs. C_D curve have been set to more effectively display the comparison between the design predictions and the experimental performance measurements across the C_L and C_D range of interest. Overall, the calculated performance of the wings from the wake survey measurements agree with those acquired from the balance measurements and the design predictions. However, as seen in Figure IV-7-Figure IV-9 b), the wake survey data has slightly higher drag than the design prediction, which was also seen in for the balance measurements in Figure IV-1.

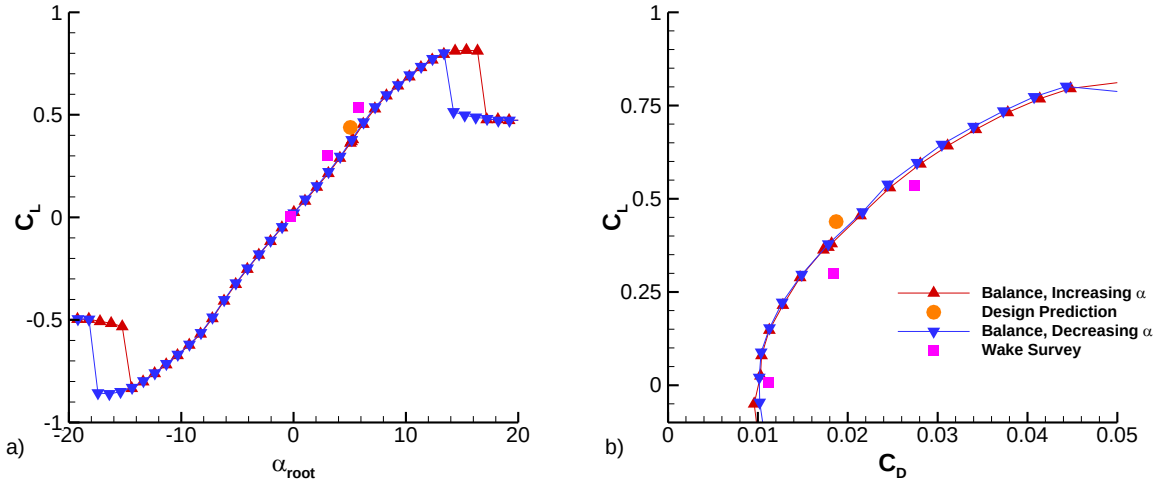

Figure IV-7 Elliptic Wing polar data compared to wake-survey data and the design predictions for a) C_L vs. α_{root} and b) detail view of C_L vs. C_D.

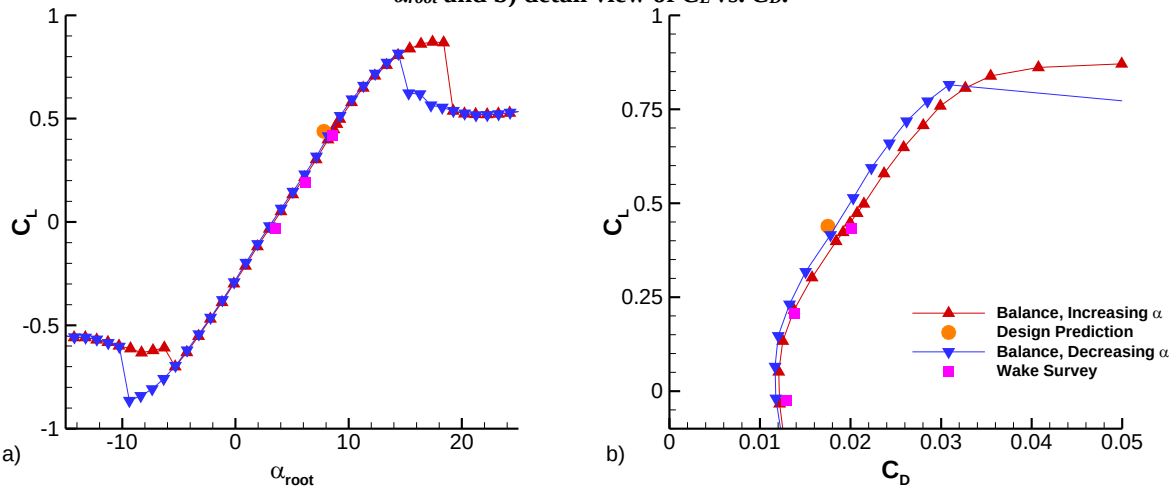

Figure IV-8 Inviscid Optimized Wing polar data compared to wake-survey data and the design predictions for a) C_L vs. α_{root} and b) detail view of C_L vs. C_D.

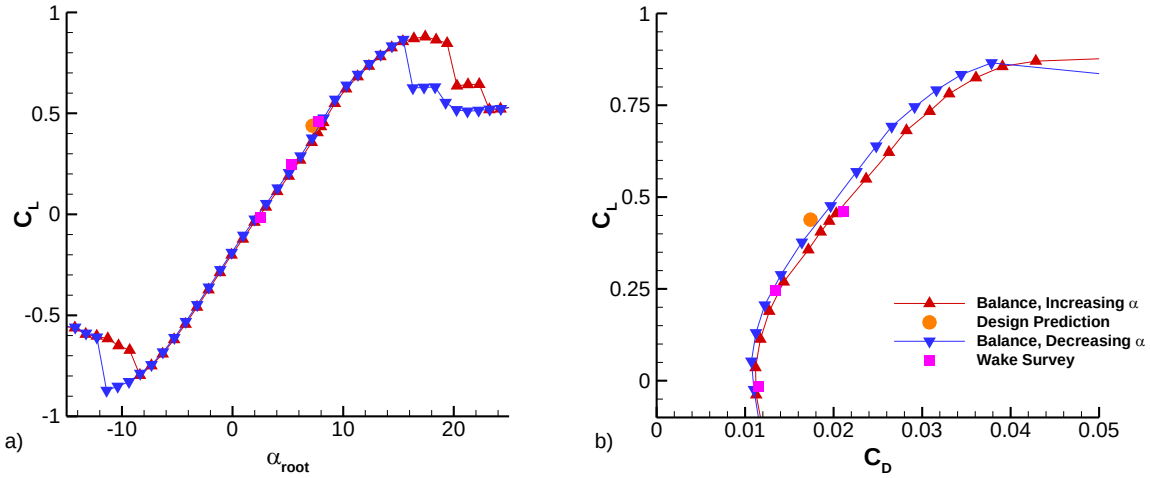

Figure IV-9 Viscous Optimized Wing polar data compared to wake-survey data and the design predictions for a) C_L vs. α_{root} and b) detail view of C_L vs. C_D.

The wake-survey measurements also display good agreement with the C_L vs. C_D polar from the balance measurements; however, there is some disparity between the lift-coefficient measurements and angle of attack setting when comparing wake-survey and balance measurements, as seen in most prominently in Figure IV-7 a). The differences between the balance measurements and the wake-survey measurements likely stem from multiple sources. The high level of distortion of the flow at the wing root due to the interaction with the junction vortex likely has an effect on the measured vorticity produced by the wing across the region near the wall, causing the wing vorticity to dissipate and spread across the wake plane. This effect can be observed by the decreased amplitude of the vorticity near the wing root and the small patches of vorticity present outside of the wake trace as observed in Figure IV-4-Figure IV-6 b). Additionally, some of the assumptions of the wake-survey method concerning the wake may not be fully valid. Since the method assumes a fixed wake, it is unable to take into account the roll-up of a wake vortex sheet and viscous dissipation of vortices, which occurs in real wing flows.

Spanwise lift distributions were also obtained for each of the three wings using the wake survey measurements. A comparison of the design and experimentally-obtained spanloads for each wing can be seen in Figure IV-10 From this comparison, it can be seen that the general trend of the lift distribution is consistent between the design and the experiment, though there is a noticeable difference near the root. As discussed previously, this difference is attributed to the interaction between the shed circulation of the wing and the junction vortex or wall boundary layer. It is worth noting, however, that a junction vortex is a relatively common phenomenon on

practical aircraft applications. As a result, if a true indication of the performance of a wing is desired, linearized, inviscid modeling methods will be incapable of capturing the influence that these structures have on the aerodynamic performance of a wing. As a result, if resolving such an influence is important in the design of an aircraft, it would be necessary to incorporate higher-order approaches that include viscous effects as part of the design process.

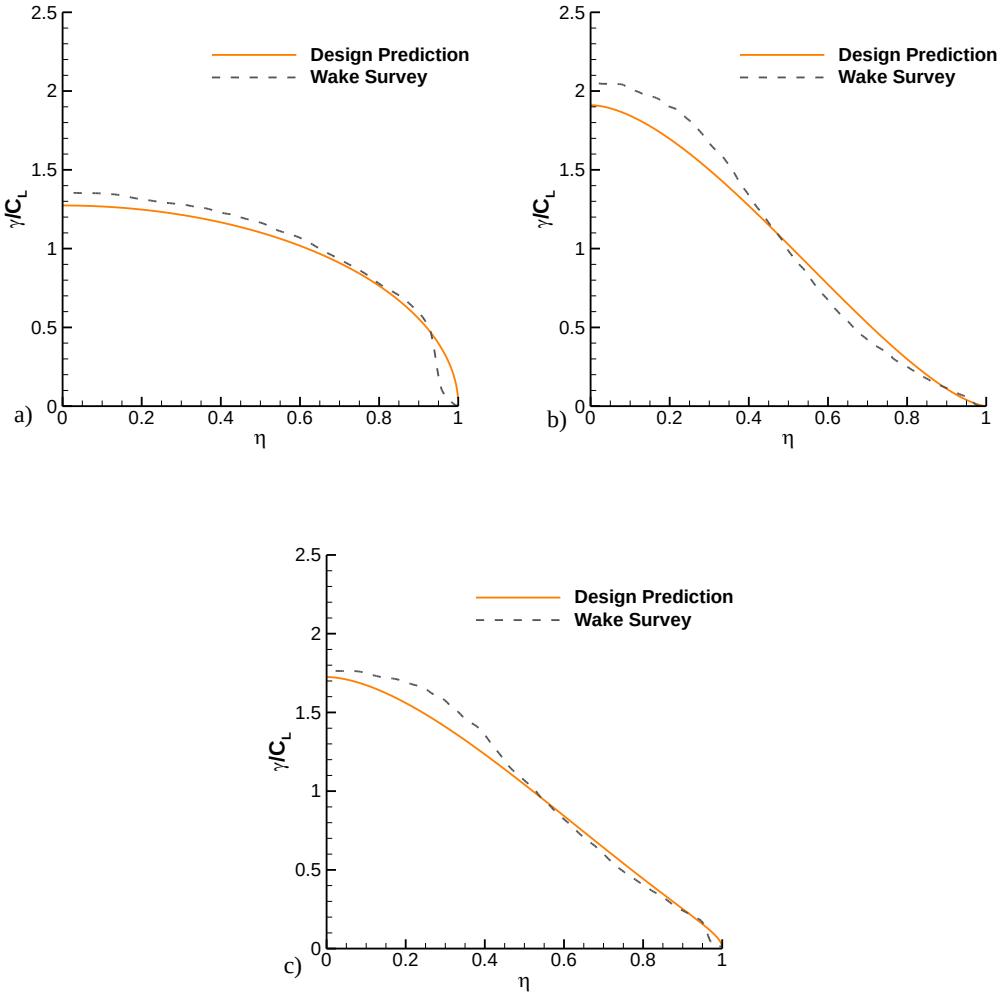

Figure IV-10 Comparison between predicted spanwise lift and that obtained experimentally from the wake survey: a) the Elliptic Wing, b) the Inviscid Optimized Wing, and c) the Viscous Optimized Wing.

It can also be observed that the outboard portions of the spanload differ from the design to different degrees for each wing. The Elliptic Wing has a significant premature decrease in lift at the tip compared to the design spanload, and this effect is visible to a lesser extent in the Viscous Optimized Wing. This sudden decrease in the spanload of the Elliptic Wing is attributed to the roll-up of the wake after leaving the wingtip. In contrast, the smallest observable tip-vortex was

exhibited in Figure IV-5 by the Inviscid Optimized Wing. As a result, in Figure IV-10 b), there appears to be no significant premature decrease in lift compared to the design. Since the Inviscid Optimized Wing features a tapering of the spanload to zero as the tip region is approached, the strength of the trailing vortex sheet at the tip is significantly weaker than that for the Elliptic Wing.

From the comparison of the wake-survey measurements to the design prediction, it can be seen that the experimental measurements vary from the design prediction to various extent, but overall that the low order design method used in this experiment is still qualitatively similar to the experimentally-obtained results. The results of this experiment demonstrate that inviscid approximations with simple, empirical viscous corrections can be used effectively in the preliminary design of wings. For the final design and analysis of wings, however, higher-order methods would be useful to resolve viscous-based complex interactions.

V. Conclusions

This work documents the findings of a study on planar wings designed with optimum spanloads for minimum drag under a fixed wing-root bending moment constraint. Three wings were designed using a Lagrange multiplier optimization method, with and without incorporating a representative viscous effect. These wings were also experimentally evaluated in a wind-tunnel environment. The results of this investigation indicate that significant decreases in drag from an elliptic spanload are produced by increasing the wing span, while keeping the lift and wing-root bending moment fixed. Representing viscous effects by incorporating a profile drag term in a strip theory approach yielded a more realistic optimization problem, as total drag could be minimized instead of induced drag.

In general, the trends of the design prediction method agreed with the experimental measurements, though the theoretical model generally over-predicted the wing lift and under-predicted the wing drag. However, these differences in theoretical predictions and experimental measurements were consistent with observations in the literature for airfoils at low Reynolds numbers. 5-hole probe wake-survey measurements were used to obtain the spanwise lift distributions. These distributions allowed the designed spanload to be compared to those obtained experimentally. The qualitative agreement between the predictions and measurements indicate that while simple representations of viscous effects can be used in spanload optimization, higher fidelity methods are required to capture effects produced by more complex flow features, if desired. These complex features could include boundary layer effects of a fuselage-wing junction or, in the case of this experiment, the floor boundary layer and its effects.

Appendix A. Detailed Derivation of Wake-Survey Method from Far-field Analysis

A.1. Far-field Analysis and the Trefftz Plane

Far-field analysis allows the flow across a downstream plane to be used to compute forces acting local to a wing or lifting surface.[29] The Trefftz Plane is normal to the free-stream flow V_∞ at its location far downstream from the wing as seen in Figure A.1 as S_T. In real experiments, the Trefftz plane is the plane at which a five-hole pressure probe would collect pressure data, however, theoretically the Trefftz plane is infinitely far downstream from the wing. The induced drag and lift of the wing can be calculated using the circulation across the Trefftz plane which is shed from the wing into the wake. In this section, a derivation of induced drag using the Trefftz plane will be done to help show the basics of far-field analysis and serve as a starting point for the more complicated derivations of profile drag in the next section.

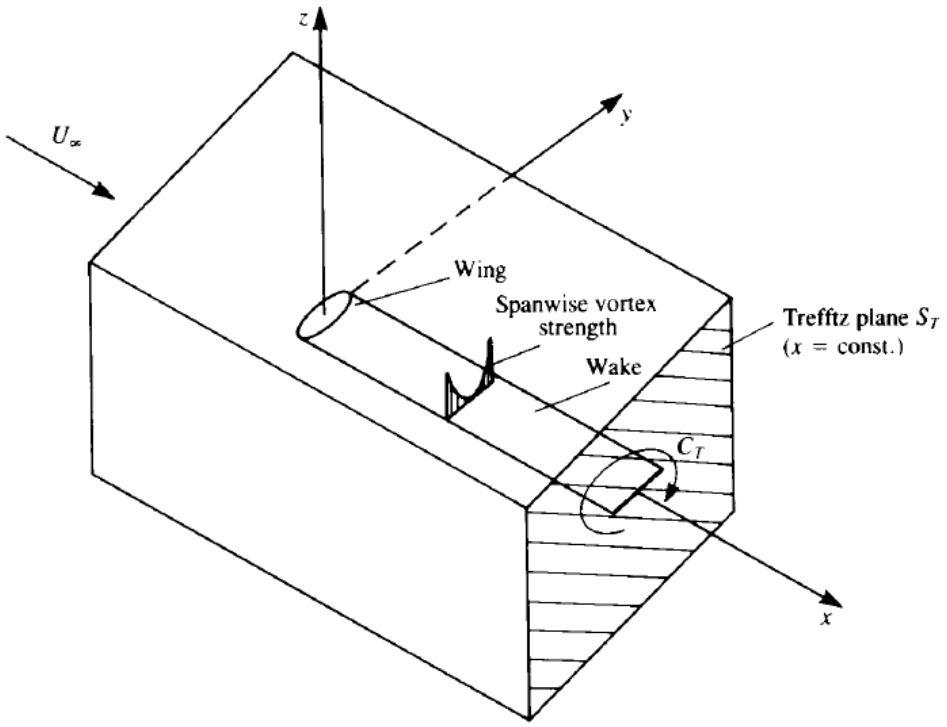

Figure A-1 Control volume used for far-field analysis conservation of momentum equation, after Katz and Plotkin.[30]

Applying conservation of momentum on the control volume for an inviscid, incompressible, steady flow where body forces are neglected results in equation (A.1).

$$\int_S \rho * \boldsymbol{V}(\boldsymbol{V} \cdot \boldsymbol{n}) dS = \boldsymbol{F} - \int_S p * \boldsymbol{n} dS \tag{A.1}$$

ρ – density

$\boldsymbol{V}$ – velocity vector

$\boldsymbol{n}$ – normal vector

p – pressure

S – control volume surface

In equation (A.1), the left hand side of the equation represents the rate of momentum outflow through the surface. The first term on the right hand side is the force acting on the fluid due to the presence of the body, and the integral term is the integral of the pressures acting on the control volume through the surface.

Letting $\boldsymbol{V} = (U_\infty + u,\ v,\ w)$ where u, v, and w are the perturbation velocities in the x, y, and z directions respectively, the drag equation (A.2) can be determined when the x-component of (A.1) is computed.

$$D = -\int_S \rho(V_\infty + u)[(V_\infty + u)\, dydz + v\, dxdz + w\, dxdy] - \int_S p\, dydz \tag{A.2}$$

Equation A.3 can be used with the control volume analysis as subtracting P_∞ from all surfaces cancels to zero. Bernoulli's equation can be used to find pressures in equation A.4 since the flow is both inviscid and incompressible:**Error! Bookmark not defined.**

$$\int_S p\, dydz = \int_S (p - p_\infty)\, dydz \tag{A.3}$$

$$p - p_\infty = \frac{\rho}{2} V_\infty^2 - \frac{\rho}{2}[(V_\infty + u)^2 + v^2 + w^2] = -\rho\, u\, V_\infty - \frac{\rho}{2}(u^2 + v^2 + w^2) \tag{A.4}$$

The results from (A.3) and (A.4) can be substituted back into (A.2) which results into a new drag integral:[29]

$$D = \int_S \frac{\rho}{2}(u^2 + v^2 + w^2)\, dydz - \int_S \rho(V_\infty + u)V_\infty dydz + \int_S \rho u V_\infty dydz \tag{A.5}$$

$$- \int_S \rho(V_\infty + u)[u\, dydz + v\, dxdz + w\, dxdy]$$

Neglecting second order terms ($u^2 \approx 0, uv \approx 0, uw \approx 0$), the first and fourth integral can be simplified. As a result, the fourth integral reduces to (A.6), which then reduces to zero because of continuity $\int_S \rho(\boldsymbol{V} \cdot \boldsymbol{n})dS = 0$.[29]

$$\int_S \rho V_\infty (u\, dydz + v\, dxdz + w\, dxdy) = 0 \tag{A.6}$$

The second and third terms can be combined to simplify to (A.7) which will cancel out when integrated across the control volume, as all terms are constant:

$$- \int_S \rho V_\infty^2 dydz = 0 \tag{A.7}$$

As a result of (A.6) and (A.7), the drag equation is reduced:

$$D = \frac{\rho}{2} \int_S (u^2 + v^2 + w^2) dydz \tag{A.8}$$

However, as the flow had been assumed inviscid, the flow in the wake is parallel to the free stream flow, which implies that there will only be velocity perturbations in the y and z directions: $u^2 \ll v^2, w^2$. Since the perturbation velocity in the streamwise direction would provide the viscous momentum deficit associated with profile drag, the Trefftz plane analysis does not provide a measurement for evaluating profile drag contributions.[29] It is also assumed that the $\pm y$ and $\pm z$ boundaries of the control volume are infinitely far from the wing. Thus, only on the Trefftz Plane are the values for v and w nonzero, so the drag integral equation can be taken only across S_T.[27]

$$D = \frac{\rho}{2} \int_{S_T} (v^2 + w^2) dydz \tag{A.9}$$

The integral in equation (A.9) as identified by Betz as the induced drag in his formulation of drag which was further used by Maskell to define induced drag in terms of vorticity and scalar functions in the wake of a wing (See equation (A.18)).

A.2. Profile Drag from Betz and Maskell

The theories of Maskell and Betz allow the profile drag to be calculated from wake-survey variables. In using these theories, the area where data is captured can be minimized as only measurements across the wake trace need to be captured.[25] Reducing the amount of area needed for capture is essential, as wake-survey experiments are typically very long as several thousand data points need to be captured.

There are a few assumptions that need to be formalized before beginning with the drag calculations based on the theory of Betz and Maskell. First, the incoming flow at the front of the control volume needs to satisfy the undisturbed free stream condition. As a result, this plane of the control volume should be relatively far upstream of the model. Secondly, all of the data captured during the wake-survey test needs to be taken from only one plane behind the model. Third, the Mach number in the tunnel is limited to 0.5 because of the flow at the wake-survey station being assumed steady and incompressible.[31] Fourth, the surfaces of the control volume are assumed to be solid and represent the wind tunnel walls; as a result, blowing and suction cannot be incorporated in this analysis. Fifth, the walls are assumed parallel, and the tunnel freestream velocity is, as a result, tangent to the tunnel wall surfaces everywhere in the flow.[31] Finally, the viscous shear stresses at the wake-survey station are to be neglected.[25]

As was stated earlier, the forces that act on the model can be evaluated from flow variables measured at the wake-survey plane. As was done in the previous section, the drag is able to be calculated from the change in momentum across the x-direction of the control volume, as seen in Figure A.2.

The drag can be written as the difference between momentum at S_1 and S_2 (upstream and downstream planes) as seen in equation (A.10).

$$D = \iint_{S_1} (p + \rho u^2) dy dz - \iint_{S_2} (p + \rho u^2) dy dz \tag{A.10}$$

Total pressure is introduced as p_t:

$$p_t = p + \frac{\rho}{2}(u^2 + v^2 + w^2) \tag{A.11}$$

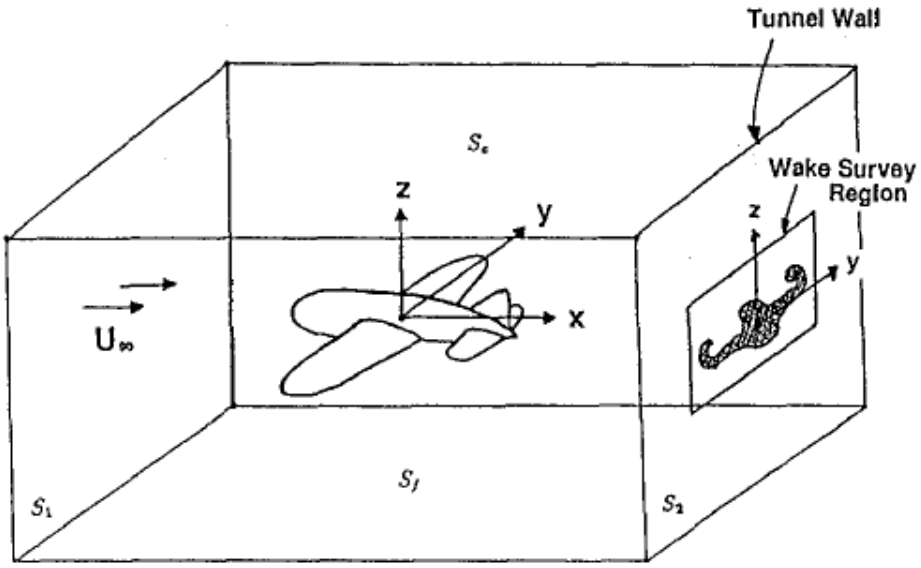

Figure A-2 Control volume and coordinate system used to derive drag based on the theories of Betz and Maskell, after Kusunose.[31]

Using p_t and the fact that the flow at S_1 satisfies the undisturbed free stream condition, equation A.10 can be rewritten as:[31]

$$D = \iint_{W_A} (p_{t,\infty} - p_t)dydz + \frac{\rho}{2}\iint_{S_2} (V_\infty^2 - u^2 + v^2 + w^2)dydz \tag{A.12}$$

W_A - the wake survey area

$p_{t,\infty}$- the total freestream pressure

Notice that the first integral is limited to an integral only over the wake area since there is no loss in total pressure outside the wake as there $(p_t = p_{t,\infty})$.[31]

In order to limit the second integral in equation (A.12) to an integral over the wake area only, Betz introduced u^*, an artificial velocity component that is different from *u* in the wake area alone.[27] The equation for the artificial velocity is seen below and is similar to equation (A.11):

$$p_{t,\infty} = p + \frac{\rho}{2}(u^{*2} + v^2 + w^2) \tag{A.13}$$

A perturbation velocity (u') in the x-direction is now to be defined as:[31]

$$u' = u^* - V_\infty \tag{A.14}$$

Now, using equations (A.13) and (A.14) the drag equation (A.12) now becomes:

$$D = \iint_{W_A} \left[\left(p_{t,\infty} - p_t\right) + \frac{\rho}{2}(u^* - u)(u^* + u - 2V_\infty) \right] dydz + \frac{\rho}{2} \iint_{S_2} (v^2 + w^2) dydz - \frac{\rho}{2} \iint_{S_2} u'^2 dydz \tag{A.15}$$

The integrals above were first derived by Maskell,[26] but the first integral of (A.15) was seen as an expression for profile drag by Betz, and he saw the second integral as an expression for induced drag as mentioned in the discussion around equation (A.9) which is identical to this second integral.[27]

In order to deal with the last integral of equation (A.15) and express the x-direction perturbation velocity in an integral over the wake survey area, Maskell introduced u_b, the wake blockage velocity:[26]

$$u_b = \frac{1}{2S_{TS}} \iint_{W_A} (u^* - u) dydz \tag{A.16}$$

Where S_{TS} represents the wind tunnel cross-sectional area.

According to Kusunose,[31] equation (A.16) allows for the third integral of (A.15) to be transformed as seen below:

$$\frac{\rho}{2} \iint_{S_2} u'^2 dydz = \rho u_b \iint_{W_A} (u^* - u) dydz \tag{A.17}$$

Since this integral is now in the form of a wake integral, it can be combined with the first integral of equation (A.15), which results in the final "total drag" equation (A.18).

$$D = \iint_{W_A} \left[\left(p_{t,\infty} - p_t\right) + \frac{\rho}{2}(u^* - u)\{u^* + u - 2(V_\infty + u_b)\} \right] dydz + \frac{\rho}{2} \iint_{S_2} (v^2 + w^2) dydz \tag{A.18}$$

$$D_{profile} = \iint_{W_A} \left[\left(p_{t,\infty} - p_t\right) + \frac{\rho}{2}(u^* - u)\{u^* + u - 2(V_\infty + u_b)\} \right] dydz \tag{A.19}$$

$$D_{induced} = \frac{\rho}{2} \iint_{S_2} (v^2 + w^2) dydz \tag{A.20}$$

Equation A.18 represents the final expression for calculating drag using the far-field method. Profile drag, as expressed in equation (A.19) can be completely determined by flow variables capture in the wake area. However, the induced drag expression is still an integral over the entire plane surface. In the next section there is a discussion on how Maskell was able to introduce a method that allows the induced drag integral expression to be reduced to an integral over the wake area as opposed to the entire plane. This formulation will be discussed in the next section.

A.3. Induced Drag from Maskell

In order to determine an equation for induced drag that uses measurements acquired across the wake trace alone, Maskell utilized two scalar functions: ξ, the x-component of the vorticity vector, and σ, the source strength, which is defined using the continuity equation.[26] These functions can be defined in terms of the cross-sectional velocities v and w, which can be measured in the wake. The definitions for these scalar functions are seen in equations (A.21) and (A.22).

$$\xi = \frac{\partial w}{\partial y} - \frac{\partial v}{\partial z} \tag{A.21}$$

$$\sigma = \frac{\partial v}{\partial y} + \frac{\partial w}{\partial z} \tag{A.22}$$

Two more scalar functions are also defined which satisfy the vorticity equation (A.21) and the source equation (A.22). These functions are $\psi(y,z)$ and $\phi(y,z)$ and can be seen below:

$$v = \frac{\partial \psi}{dz} + \frac{\partial \phi}{\partial y} \tag{A.23}$$

$$w = -\frac{\partial \psi}{\partial y} + \frac{\partial \phi}{\partial z} \tag{A.24}$$

According to Brune[25], the following equations determine ψ and ϕ:

$$\frac{\partial^2\psi}{\partial y^2}+\frac{\partial^2\psi}{\partial z^2}=-\xi \tag{A.25}$$

$$\frac{\partial^2\phi}{\partial y^2}+\frac{\partial^2\phi}{\partial z^2}=\sigma \tag{A.26}$$

Equation (A.25) is only true along the streamlines inside of the wake.[31] It must also satisfy a boundary condition at the tunnel walls in order to ensure that the walls become streamlines of the flow field: $\psi_{wall}=0$. Equation (A.26) is also configured with a boundary condition of $\left(\frac{\partial\phi}{\partial n}=0\right)$ in order to ensure the tunnel walls are considered solid boundaries and no flow passes through them.

Using the definitions in equations (A.21-A.26), the induced drag equation can be re-written:

$$D_i=\frac{\rho}{2}\iint_{S_2}(v^2+w^2)dydz=\frac{\rho}{2}\iint_{W_A}\psi\xi\ dydz-\frac{\rho}{2}\iint_{S_2}\phi\sigma\ dydz \tag{A.27}$$

The second term is still an integral over the entire surface S_2. However, wake measurements taken in experiments have shown that the source term σ is small outside of the wake, allowing the $\phi\sigma$ term to be neglected everywhere except inside the wake region.[25] This allows induced drag to be approximated by the following integral:

$$D_i\approx\frac{\rho}{2}\iint_{W_A}(\psi\xi-\phi\sigma)\ dydz \tag{A.28}$$

The above equation is the result reached by Brune[25]; however, Kusunose[31] cites the work by De Leeuw to simplify the equation further. De Leeuw conducted experiments with a half-wing model in a wind tunnel, and found that the $\phi\sigma$ term in equation (A.28) contributes very little to the total drag. As a result, the induced drag equation can be simplified further:

$$D_i\approx\frac{\rho}{2}\iint_{W_A}\psi\xi\ dydz \tag{A.29}$$

A.4. Lift from the Wake-survey Method

If the control volume of Figure A.2 is revisited, lift as a function of flow variables can be found. If conservation of momentum is applied in the z-direction, the lift on the wing can be written:

$$L = \iint_{S_f} p\, dxdy - \iint_{S_C} p\, dxdy - \rho \iint_{S_2} uw\, dydz \tag{A.30}$$

In equation (A.30), the first two terms are the static pressure integrals of the floor and ceiling, respectively. The third term is an integral over the surface S_2, the wake-survey plane. This integral represents the effect of downwash behind the model. Using vorticity and u^*, Maskell was able to represent lift in terms of integrals over W_A.[26]

$$L = \rho U_\infty \iint_{W_A} y\xi\, dudz + \rho \iint_{W_A} (u^* - u)w\, dydz \tag{A.31}$$

The effect of the second term in equation (A.29) is considered effectively negligible, so lift can be approximated without it.[26]

$$L \approx \rho U_\infty \iint_{W_A} y\xi\, dudz \tag{A.32}$$

The above equation is Maskell's result for lift. However, Kusunose also puts forth a method using classical circulation theory that can be compared to equation (A.30). The equations used for this method can be seen below. A diagram of the shed circulation across the far-field plane and relevant variables are also shown in is Figure A.3 after Kusunose.[31]

$$L = \rho U_\infty \int_{y_L}^{y_R} \Gamma(y) dy \tag{A.33}$$

$$\Gamma(y) = \begin{cases} -\Gamma_L(y) = + \int_{y_L}^{y} \gamma(y) dy \\ -\Gamma_R(y) = - \int_{y}^{y_R} \gamma(y) dy \end{cases} \tag{A.34}$$

$$\gamma(y) = - \int_{z_{W_A}} \xi(y, z) dz \tag{A.35}$$

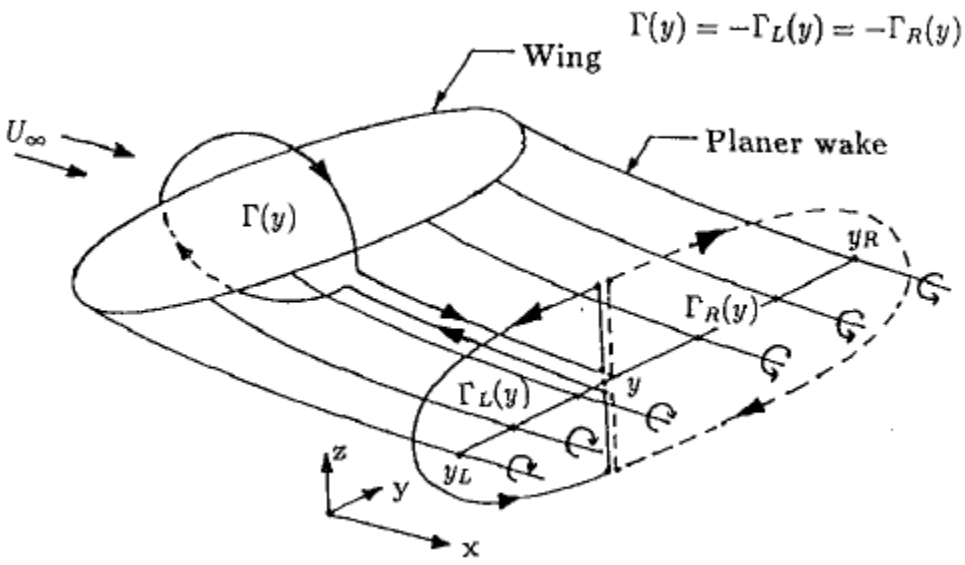

Figure A-3 A wing and its planar wake: a visual representation of Kelvin's circulation theorem, after Kusunose.[31]

This second method detailed in equations (A.33-A.35) incorporates a planar wake assumption to determine spanwise lift. As the tips of wing wake roll up in real flow, the lifting characteristics on the wing cannot be perfectly reconstructed. As a result, the lift distribution in this vicinity cannot be exactly determined and errors can accumulate near the regions of the wing tips.[31]

Appendix B. Five-Hole Probes: Theory of Operation and Calibration

In order to capture the pressure data necessary to calculate velocities, vorticity, and other necessary terms, five-hole pressure probes are used. Pressure probes are in-flow pressure measurement devices and can capture pressure data directly. In general, pressure tubes and probes can be classified as follows:[32]

- *Static tubes* are used to measure local static pressure
- *Pitot tubes* are used to measure local total pressure
- *Pitot-static tubes* are combinations of pitot and static tubes and can provide the local dynamic pressure, from which local flow velocity can be obtained
- *Multi-hole probes* are combinations of pitot and static tubes, five-hole probes are most common, and these probes can be used to provide local static, total, and dynamic pressure as well as the three components of the local velocity vector.

Pressure tubes are typically low resolution, spatially and temporally. However, very small pressure transducers can be installed within a pressure probe near the ports that can allow for fast response times and increase the resolution of the data.

For the typical wake-survey experiment, like those conducted or referenced by Brune[25] and Kusunose[31] five-hole pressure probes are most commonly used. There are reasons to choose between the typical five-hole probe, or a fast response probe, or a seven+ hole probe, through the choice largely depends on the needs of the experiment.

Multi-hole probes are used specifically so that the data they capture can help the researcher determine the flow velocity vector, or rather, the magnitude and direction of the flow. Five-hole probes incorporate five parallel tubes, one in the center with the hole normal to the tube body, surrounded by four others in a pyramid or conical tip shape. The probe is symmetric and an example can be seen in Figure B.1.

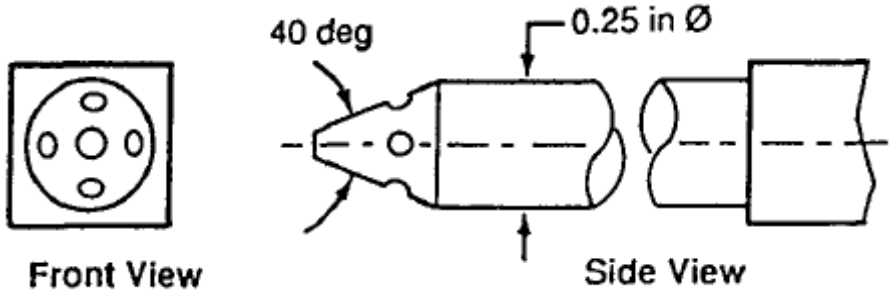

Figure B-1 Five-hole probe front and side views after Kusunose.[31]

The probes used by Boeing in the 1990s were like the one seen in Figure B.1. They were run in non-nulling mode, which allows for faster acquisition of data. According to Brune[25], the pneumatic probes like the one seen in Figure B.1 provide three main benefits. First, they can measure all three components of velocity in the wake as well as total pressure, and they can make these measurements accurately and simultaneously. Second, the data is time averaged automatically, reducing the data output and post-processing time.[25] Finally, compared to other in-flow measurements like hot wire anemometers, pneumatic probes are far more durable and less likely to break or become contaminated by particles in the wind tunnel.[25] Because of these benefits, only one five-hole pressure probe is necessary to use in experiments; however, more than one would reduce testing time and costs. Despite the benefits of using multi-hole probes in wake-survey experiments, it is worth noting that five-hole probes may be affected by Reynolds number, shear flow, vibration, misalignment, proximity to walls, the presence of turbulence or of compressible flows.[32]

The probes are typically mounted to a traverse system, which can move in a Cartesian grid space, or can sweep in semi-circular arcs. For most tests, the probes would be parallel to the tunnel walls. An example of a wake-survey area that would be captured by a five-hole pressure probe during an experiment is modeled in Figure B.2, after Brune.[25]

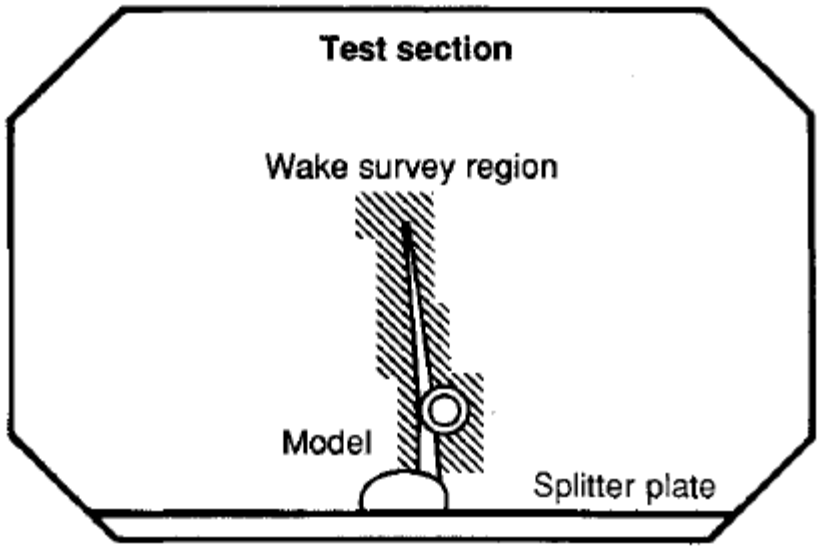

Figure B-2 An example of a wake-survey region after Brune.[25]

The following five-hole probe calibration method is carried out in MATLAB and is based upon the work of Diebold.[33] Initially, a calibration data set is taken. The pressure probes must be calibrated to map the acquired 5-port pressure measurements to total and static pressures and three-component velocities. The calibration procedure involves the pressure probes being placed in a uniform free stream flow inside of the empty wind tunnel. The probes are angled at different combinations of pitch, α_p, and yaw, β_p. The five pressures are then recorded. The numbering scheme for this analysis can be seen in Figure B.3.

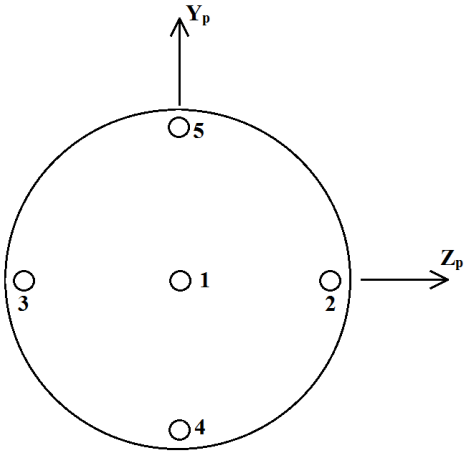

Figure B-3 Labeling scheme for five-hole pressure probes to be used in calibration discussion.[33]

An average pressure p_m is calculated:

$$p_m = \frac{1}{4}(p_2 + p_3 + p_4 + p_5) \tag{B.1}$$

The pitch pressure coefficient can now be calculated:

$$C_\alpha = \frac{p_4 - p_5}{p_1 - p_m} \tag{B.2}$$

The yaw pressure coefficient:

$$C_\beta = \frac{p_3 - p_2}{p_1 - p_m} \tag{B.3}$$

The total pressure calibration coefficient at the tip of the probe:

$$C_{PT} = \frac{p_1 - p_{total}}{p_1 - p_m} \tag{B.4}$$

The static pressure calibration coefficient at the tip of the probe:

$$C_{PS} = \frac{p_m - p_{static}}{p_1 - p_m} \tag{B.5}$$

Unfortunately, p_{total} and p_{static} are not measured directly during data acquisition. However, this can be resolved since all acquired pressure measurements are referenced against the static pressure of the tunnel test section. As $p_{total} - p_{ts} = q_{\infty}$, the total pressure coefficient can be calculated as follows:

$$C_{PT} = \frac{p_1 - q_{\infty}}{p_1 - p_m} \tag{B.6}$$

Similarly, static pressure referenced against itself is zero, so the static pressure coefficient can be re-written as:

$$C_{PS} = \frac{p_m}{p_1 - p_m} \tag{B.7}$$

Next, the calibration values of C_{α} and C_{β} are used to create linearly spaced vectors, and then assembled into a rectangular grid in 2D space using the MATLAB functions linspace and meshgrid. The linearly spaced vector forms of C_{α} and C_{β} are used in conjunction with the scatteredInterpolant function in MATLAB to create interpolants (interpolating functions that can be evaluated at desired locations) for the probe pitch, α_p, and yaw, β_p, angle data as well as the C_{PT} and C_{PS} data. These interpolants are represented by the F's in (B.8-B.11).

$$\alpha_p = F_{\alpha}(C_{\alpha}, C_{\beta}) \tag{B.8}$$

$$\beta_p = F_{\beta}(C_{\alpha}, C_{\beta}) \tag{B.9}$$

$$C_{PT} = F_{PT}(C_{\alpha}, C_{\beta}) \tag{B.10}$$

$$C_{PS} = F_{PS}(C_{\alpha}, C_{\beta}) \tag{B.11}$$

These functions can be used now in conjunction with experimental five-hole probe pressure data. Experimental data is taken where the pitch and yaw angles of the flow are unknown. In order to reduce the five-hole probe pressure data into the three components of velocity, these angles are necessary. By calculating experimental values of C_{α} and C_{β}, the experimental angles can be found as well as the experimental total and static pressure calibration coefficients, which can be used to find total and static pressure coefficients.

Appendix C. Wake Survey Data Reduction Methods

The data reduction code used to reduce the wake survey experimental data was created in MATLAB based on the work of Diebold.[33] The code was used to apply calibration data to the experimental five-hole probe pressure data, allowing for experimental values of probe pitch, α_p, and yaw, β_p to be determined as well as the experimental C_{PT} and C_{PS}. These values were found by calculating B.2 and B.3 for the experimental data, and then using the calibration interpolant functions from B.8-B.11. Using these experimental calibration coefficients and the measured dynamic pressure and tunnel freestream velocity, the experimental total pressure, static pressure, and total local velocity were found using the equations C.1-C.5 at each measurement location.

$$p_{total} = \left(p_1 - C_{PT}(p_1 - p_m)\right) \tag{C.1}$$

$$C_{p,t} = \frac{p_{total}}{q_\infty} \tag{C.2}$$

$$p_{static} = \left(p_m - C_{PS}(p_1 - p_m)\right) \tag{C.3}$$

$$C_{p,s} = \frac{p_{static}}{q_\infty} \tag{C.4}$$

$$V_{tot} = U_\infty \sqrt{C_{p,t} - C_{p,s}} \tag{C.5}$$

The three components of velocity are able to be extracted from the total local velocity using the experimental values of probe pitch, α_p, and yaw, β_p angles. First, the values of wing pitch α_w, and yaw, β_w need to be determined, as they are different from the probe angles. The relation between these angles can be seen in equations C.6 and C.7.

$$\alpha_w = \beta_p \tag{C.6}$$

$$\beta_w = \alpha_p \tag{C.7}$$

Now the three components of velocity can be found using these angles and the total local velocity as seen in equations C.8-C.10.

$$u = V_{tot}\cos(\beta_w)\cos(\alpha_w) \tag{C.8}$$

$$v = V_{tot}\sin(\beta_w) \tag{C.9}$$

$$w = V_{tot}\cos(\beta_w)\sin(\alpha_w) \tag{C.10}$$

The next step is to interpolate the experimental data into a grid with step size equal to the smallest experimental step size, 0.125 in. The data that was interpolated into a grid was the total

local velocity V_{tot}, the axial velocity component u, the spanwise velocity component v, and the normal velocity component w. Additionally, the total pressure coefficient $C_{p,t}$, dynamic pressure q_∞, and freestream velocity V_∞ were interpolated to the grid. The data was smoothed using Savitzky-Golay filtering on the velocity and total pressure distributions before finite difference techniques were used to compute vorticity using equation III.25 and the *y*- and *z*-derivatives of the total pressure difference from the freestream value. The total pressure difference was defined as $1 - C_{p,t}$. The *z*-derivative of the total pressure difference was used in order to find the position of the wake, as the presence of the wake creates a rapid change in total pressure with respect to the z-direction. The total pressure and velocity measurements outside of the wake trace were then neglected in the calculation of lift and drag components, including the portion of the flowfield dominated by a wing-floor juncture vortex, where portions of vorticity were also neglected from the lift and drag calculations.

The MATLAB code then calculated lift and lift coefficient using the method developed by Maskell from equation III.20. Additionally, circulation, lift, and spanwise lift coefficient were calculated using circulation theory (equations III.23 & III.24).

In order to calculate induced drag from equation III.19, the stream function needs to be found in from the Poisson equation seen in C.11. The stream function ψ is found using a discrete Poisson solver using the negative vorticity.

$$\frac{\partial^2 \psi}{\partial y^2} + \frac{\partial^2 \psi}{\partial z^2} = -\xi \tag{C.11}$$

This equation is solved following the method outlined by Diebold[33] using the tunnel wall boundary condition that, at the walls, $\psi = 0$. In order to use this boundary condition, the computational grid was extended from the wake survey area of the tunnel test section walls. In the area outside of the wake, the vorticity values were equal to zero. The Poisson equation was solved using a second order central finite differencing method seen in C.12.

$$\frac{\psi_{i,j+1} - 2\psi_{i,j} + \psi_{i,j-1}}{\Delta y^2} + \frac{\psi_{i+1,j} - 2\psi_{i,j} + \psi_{i-1,j}}{\Delta z^2} = -\xi_{i,j} \tag{C.12}$$

Because the grid spacing was equidistant in both the z and y directions, one gap size *d* can be used in place of the z and y step sizes. The Poisson equation in C.12 was thereby solved, with an initial guess of $\psi_{i,j} = 0$ for all points in the domain, using a Jacobi iteration method.

$$\psi_{i,j}^{new} = \frac{1}{4}\left(\psi_{i+1,j}^{old} + \psi_{i-1,j}^{old} + \psi_{i,j+1}^{old} + \psi_{i,j-1}^{old} - d^2\xi_{i,j}\right) \tag{C.13}$$

An error tolerance was defined and the program was run until the difference between the most recent two iterations of $\psi_{i,j}^{new}$ was less than the error tolerance for all points in the domain. If the difference was greater than the error tolerance, the "new" data was defined as next iterations "old" data: $\psi_{i,j}^{old} = \psi_{i,j}^{new}$.

Using the calculated stream function and vorticity values, induced drag could be then found by equation A.29.

The following two equations are used to calculate u_b, the wake-blockage velocity, and u^*, an artificial velocity component, which are necessary in order to solve for the profile drag.

$$u^* = \sqrt{u^2 - V_\infty^2 * \left(1 - C_{p,t}\right)} \tag{C.14}$$

$$u_b = \frac{1}{2S_{Tunnel}} \iint_{W_A} \left(u^* - u\right) dydz \tag{C.15}$$

The profile drag is then found using equation A.19.

The wing-root bending moment coefficient was found using the following two equations:

$$C_b(y) = \left(\frac{1}{S/2}\right) C_l(y) c(y) y \tag{C.16}$$

$$\frac{b}{2} C_B = \int_0^{b/2} C_b(y)\,\mathrm{dy} \tag{C.17}$$

Appendix D. Uncertainty Analysis

In order to estimate the potential error present in this experiment, an uncertainty analysis was performed. The estimated uncertainty of some result *R*, where *R* is the function of several independently measured variables (x_i), depends on the uncertainty of each variable.

$$R = R(x_1, \ldots, x_n) \tag{D.1}$$

The uncertainty calculations follow that of Coleman and Steele[34] and assumed that the uncertainties of each measured variable were independent of each other. The experimental uncertainty (U_R) of *R* is given as the square root of the sum of the squares of each independent variable uncertainty component:

$$U_R = \sqrt{\left(\frac{\partial R}{\partial x_1} U_{x_1}\right)^2 + \cdots + \left(\frac{\partial R}{\partial x_n} U_{x_n}\right)^2} \tag{D.2}$$

An alternative expression for equation D.2 can be seen in equation D.3 if R is a product of independent variables $\left(R = k x_1^{\alpha} x_2^{\beta} \ldots x_n^{\zeta}\right)$ where k is a constant and the exponents are $\alpha, \beta, \ldots \zeta$.

$$\frac{U_R}{R} = \sqrt{\alpha^2 \left(\frac{U_{x_1}}{x_1}\right)^2 + \cdots + \zeta^2 \left(\frac{U_{x_n}}{x_n}\right)^2} \tag{D.3}$$

Using equation D.3, the uncertainty for the results from the force balance performance coefficients can be found. Equations III.10-III.12 provide the basis for the uncertainty calculation where the results (*R*) are C_L, C_D, and C_M. The relative uncertainty calculations for each of these results are seen in equations D.4-D.6.

$$\frac{U_{C_L}}{C_L} = \sqrt{\left(\frac{U_L}{L}\right)^2 + \left(\frac{U_{q_\infty}}{q_\infty}\right)^2 + \left(\frac{U_b}{b}\right)^2 + \left(\frac{U_{c_g}}{c_g}\right)^2} \tag{D.4}$$

$$\frac{U_{C_D}}{C_D} = \sqrt{\left(\frac{U_D}{D}\right)^2 + \left(\frac{U_{q_\infty}}{q_\infty}\right)^2 + \left(\frac{U_b}{b}\right)^2 + \left(\frac{U_{c_g}}{c_g}\right)^2} \tag{D.5}$$

$$\frac{U_{C_M}}{C_M} = \sqrt{\left(\frac{U_{M_{\frac{C}{4}}}}{M_{\frac{C}{4}}}\right)^2 + \left(\frac{U_{q_\infty}}{q_\infty}\right)^2 + \left(\frac{U_b}{b}\right)^2 + 4\left(\frac{U_{c_g}}{c_g}\right)^2} \tag{D.6}$$

In these equations U_L, U_D, and $U_{M_{\frac{C}{4}}}$ are the absolute uncertainties in the measured lift, drag, and pitching moment. In order to find these absolute uncertainties, equation D.2 was used to

form equations D.7-D.9 which are functions of the absolute uncertainties of the measured normal force $\left(U_{F_N}\right)$, axial force $\left(U_{F_A}\right)$, and quarter-chord pitching moment $(U_{M_{\frac{c}{4}}})$, as well as (U_α), the absolute uncertainty of the angle of attack.

$$U_L = \sqrt{\left(U_{F_N}\cos(\alpha)\right)^2 + \left(U_{F_A}\sin(\alpha)\right)^2 + (-DU_\alpha)^2} \tag{D.7}$$

$$U_D = \sqrt{\left(U_{F_N}\sin(\alpha)\right)^2 + \left(U_{F_A}\cos(\alpha)\right)^2 + (LU_\alpha)^2} \tag{D.8}$$

$$U_{M_{\frac{c}{4}}} = \sqrt{(U_M)^2 + \left(F_N U_{X_{off}}\right)^2 + \left(F_A U_{Y_{off}}\right)^2} \tag{D.9}$$

The independent variables, example reference values, and example absolute and relative uncertainties can be seen below in Table D-1.

Table D-1 Uncertainty Analysis Quantities

Independent Variable	**Reference Value (R)**	**Absolute Uncertainty, (U_R)**	**unit**	**Relative Uncertainty (%)**
b, span	1.5	0.0004	ft	0.028
c_g, mean geometric chord	0.462	0.0004	ft	0.090
F_N, normal force	7.136	0.0180	lbs	0.199
F_A, Axial Force	0.301	0.0054	lbs	1.144
M, Moment about center of balance	0.048	0.0225	ft-lbs	3.804
α, angle of attack	5.1	0.0200	deg	0.392
X_{off}, x-dir. Offset	0	0.0004	ft	
Y_{off}, y-dir. Offset	0	0.0004	ft	
q_∞, dynamics pressure	0.186	0.0004	psi	0.220
L, lift	7.081	0.0002	lbs	0.002
D, drag	0.335	0.0032	lbs	0.946
$M_{\frac{c}{4}}$, quarter-chord pitching moment	0.048	0.0228	ft-lbs	3.857
C_L, lift coefficient	0.382	0.0012		0.239
C_D, drag coefficient	0.018	0.0002		0.975
C_M, moment coefficient	-0.005	-0.0026		3.868

References

[1] Nygren, E., Aleklett, K., and Höök, M., "Aviation Fuel and Future Oil Production Scenarios," *Energy Policy*, Vol. 37, 2009, pp. 4003-4010.
[2] United States Government Accountability Office, "Aviation and Climate Change," GAO-09-554, 2009.
[3] IPCC (2014). "Climate Change 2014: Mitigation of Climate Change." Cambridge University Press, Cambridge, United Kingdom, 2014.
[4] Walsh, J.L., Weston, R. P., Samareh, J. A., and Mason, B. H., "Multidisciplinary High-Fidelity Analysis and Optimization of Aerospace Vehicles, Part 2: Preliminary Results," AIAA 2000-0419, *38th Aerospace Sciences Meeting & Exhibit*, Reno, Nevada, January 2000.
[5] McCormick, B. W., *Aerodynamics, Aeronautics, and Flight Mechanics*, John Wiley & Sons, Inc., Canada, 1995.
[6] Prandtl, L., "Applications of Modern Hydrodynamics to Aeronautics," NACA TR-116, 1923.
[7] Munk, M. M., "The Minimum Induced Drag of Aerofoils," NACA TR-121, 1923.
[8] Jones, R.T., "The Spanwise Distribution of Lift for Minimum Induced Drag of Wings Having a Given Lift and a Given Bending Moment," NACA TN-2249, 1950.
[9] Klein, A. and Viswanathan, S.P., "Minimum Induced Drag of Wings with Given Lift and Root Bending Moment," *Zeitschrift fuer Angewandte Mathematik und Physik*, Vol. 24, 1973, pp. 886-892.
[10] Prandtl, L., "On Wings with Minimum Induced Drag," *Zeitschrift Flugtechnik und Motorluftschiffahrt*, Vol. 24, Nov. 1933, pp. 305–306.
[11] Klein, A. and Viswanathan, S.P., "Approximate Solution for Minimum Induced Drag of Wings with Given Structural Weight," *Journal of Aircraft*, Vol. 12, No. 2, 1975, pp. 124-126.
[12] Löbert, G., "Spanwise Lift Distribution of Forward-and Aft-Swept Wings in Comparison to the Optimum Distribution Form," *Journal of Aircraft*, Vol. 18, No. 4, 1981, pp. 496–498.
[13] McGeer, T., "Wing Design for Minimum Drag with Practical Constraints", *Journal of Aircraft*, Vol. 21, 1984, pp. 879-886.
[14] Kroo, I., "Design and Analysis of Optimally-Loaded Lifting Systems," AIAA Paper 84-2507, 1984.
[15] Verstraeten, J.G. and Slingerland, R., "Drag Characteristics for Optimally Span-Loaded Planar, Wingletted, and C Wings," *Journal of Aircraft*, Vol. 46, No. 3, 2009, pp. 962-971.
[16] Ning, S.A. and Kroo, I., "Multidisciplinary Considerations in the Design of Wings and Wing Tip Devices," *Journal of Aircraft*, Vol. 47, No. 2, 2010, pp. 534-543.
[17] Martins, J.R.R.A. and Lambe, A.B., "Multidisciplinary Design Optimization: A Survey of Architectures," *AIAA Journal*, Vol. 51, No. 9, 2013, pp. 2049-2075.
[18] Lyu, Z. and Martins, J.R.R.A., "Aerodynamic Design Optimization Studies of a Blended-Wing-Body Aircraft," *Journal of Aircraft*, Vol. 51, No. 5, 2014, pp. 1604-1617.
[19] Antoine, N.E. and Kroo, I.M., "Framework for Aircraft Conceptual Design and Environmental Performance Studies," *AIAA Journal*, Vol. 43, No. 10, 2005, pp. 2100-2109.
[20] Blackwell, J. A., Jr., "Numerical Method to Calculate the Induced Drag or Optimum Loading for Arbitrary Non-Planar Aircraft," NASA SP-405, 1976.
[21] Wroblewski, G. E. and Ansell, P. J., "Prediction and Experimental Evaluation of Planar Wing Spanloads for Minimum Drag," AIAA Paper 2016-0561.
[22] Kroo, I., "A General Approach to Multiple Lifting Surface Design and Analysis," AIAA Paper 84-2507, 1984.

[23] Drela, M. and Youngren, H., "XFOIL 6.9 User Primer," Massachusetts Institute of Technology, Cambridge, MA, 2001. Drela, M. and Youngren, H., "XFOIL 6.9 User Primer," Massachusetts Institute of Technology, Cambridge, MA, 2001.
[24]Barlow, J.B., Rae, W.H. Jr. and Pope, A., *Low-Speed Wind Tunnel Testing*, 3rd Edition, John Wiley & Sons, Inc., New York, 1999.
[25] Brune, G.W., "Quantitative Low-Speed Wake Surveys," *Journal of Aircraft*, Vol. 31, No. 2, 1994, pp. 249-255.
[26] Maskell, E.C., "Progress Towards a Method for the Measurement of the Components of the Drag of a Wing of Finite Span," Royal Aircraft Establishment, TR 72232, 1972.
[27] Betz, A., "Ein Verfahren zur direkten Ermittlung des Profilwiderstandes," *Zeitschrift für Flugtechnik und Motorluftschiffahrt*, Vol. 16, 1925, pp. 42-44.
[28] Coder, J.G. and Maughmer, M.D., "Comparisons of Theoretical Methods for Predicting Airfoil Aerodynamic Characteristics," *Journal of Aircraft*, Vol. 51, No. 1, 2014, pp. 183-191.
[29] Drela, M., *Flight Vehicle Aerodynamics,* The MIT Press, Cambridge, Massachusetts, 2014.
[30] Katz, J. and Plotkin, A., "Far-field Calculation of Induced Drag," *Low Speed Aerodynamics: From Wing Theory to Panel Methods,* McGraw-Hill Inc., New York, 1992, Chap. 8.4, pp. 233-236.
[31] Kusunose K "Development of a universal wake-survey data analysis code." AIAA-97-31757, 1997.
[32] Tavoularis, S., "In-flow Pressure Measurements," *Measurement in Fluid Mechanics*, Cambridge University Press, New York, 2005, Chap. 8.4, pp. 193-200.
[33] Diebold, J.M., "Aerodynamics of a Swept Wing with Leading-Edge Ice at Low Reynolds Number," Thesis, University of Illinois at Urbana-Champaign, Urbana, IL, 2012.
[34] Coleman, H.W. and Steele, W.G., *Experimentation and Uncertainty Analysis for Engineers*, Wiley-Interscience, New York, 1989.